

A Precision Measurement of the Weak Mixing Angle in Møller Scattering

R. Carr, B. Filippone, E.W. Hughes, J.S. Jensen, C. Jones, Yu. Kolomensky,
R.D. McKeown, D. Pripstein
California Institute of Technology, Pasadena, CA 91125

B.D. Anderson, D.M. Manley, G.G. Petratos, J.W. Watson, W.-M Zhang
Kent State University, Kent, OH 44242

G.D. Cates, T.B. Humensky, I. Kominis, K.S. Kumar*, G.W. Miller, T. Pavlin
Princeton University, Princeton, NJ 08544-0708

P. Anthony, N. DeGroot, R. Erickson, T. Fieguth, R. Pitthan, S. Rokni,
S. St. Lorant, D. Waltz, D. Whittum, M. Woods, B. Youngman
Stanford Linear Accelerator Center, Stanford, CA 94309

R. Holmes, W. Kahl, P.A. Souder
Syracuse University, Syracuse, NY 02130

L. Auerbach, E. Kaczanowicz, Z. Meziani, M. Schnee, P. Zyla
Temple University, Philadelphia, PA 19122

J-P. Chen, R. Michaels
Thomas Jefferson National Accelerator Facility, Newport News, VA 23606

G. Shapiro
University of California, Berkeley, CA 94720-7300

*Coordinator, Email: kkumar@princeton.edu, Phone: (609)258-5586

Abstract

We propose a precision measurement of the parity nonconserving left-right asymmetry in the scattering of longitudinally polarized electrons from the atomic electrons in a hydrogen target (Møller scattering) in End Station A. The asymmetry measures the effective pseudo-scalar weak neutral current coupling governing Møller scattering ($g_{ee} \equiv \rho \cdot g_{Ve} \cdot g_{Ae}$) at an average Q^2 of 0.03 (GeV/c)^2 and is proportional to $(\frac{1}{4} - \sin^2 \theta_W)$, where $\sin^2 \theta_W$ is the electroweak mixing angle. We plan to measure the asymmetry to a precision of 7×10^{-9} , which would measure g_{ee} to a relative precision of 6%, corresponding to $\delta(\sin^2 \theta_W) \sim 0.0007$. The dominant systematic error is expected to come from the measurement of the beam polarization, corresponding to $\delta(\sin^2 \theta_W)_{\text{syst}} \sim 0.0003$.

The ability to measure a purely leptonic weak neutral current coupling with such precision at low Q^2 is unprecedented. A comparison of such a measurement with precision asymmetry measurements at the Z^0 resonance would provide the first statistically significant measurement of $\sin^2 \hat{\theta}_W(M_Z^2) - \sin^2 \hat{\theta}_W(0)$, testing the electroweak theory at the quantum loop level, *for the first time away from the Z^0 resonance*. The measurement has unique sensitivity to new electron-electron interactions at the TeV scale, accessing the electron compositeness scale at the same level as the ultimate reach of LEP-200.

Contents

1	Introduction	7
2	Physics Motivation	8
2.1	Parity Violating Electron Scattering	8
2.2	Left-Right Asymmetry in Møller Scattering	9
2.3	Standard Model Radiative Corrections	11
2.4	New Physics Sensitivity	12
2.4.1	New Neutral Gauge Bosons	12
2.4.2	Other Contact Interactions	13
2.4.3	Oblique Corrections	14
3	Experimental Design	15
3.1	Polarized Beam	16
3.1.1	Electron Source	16
3.1.2	Electron Beam in ESA	17
3.2	Liquid Hydrogen Target	17
3.2.1	Design Specifications	17
3.2.2	Major Systems	18
3.3	The Spectrometer	20
3.3.1	Design Criteria	20
3.3.2	ESA Layout	21
3.3.3	Primary Beam Profile and Containment	23
3.3.4	Simulation Results	24
3.4	Calorimeter	25
3.4.1	Basic Specifications	26
3.4.2	Detector Geometry	27
3.4.3	Signal and Background Estimates	27
3.5	Electronics and Data Acquisition	28
3.5.1	Integrating ADCs	30
3.6	Beam Polarimeter	30

4	Systematic Uncertainties	31
4.1	Helicity Correlations	31
4.1.1	Intensity Feedback	31
4.1.2	Monitoring of Beam Parameters	33
4.1.3	Null Asymmetries	33
4.2	Longitudinal Beam Polarization	35
4.3	Physics Backgrounds	35
4.4	Radiative Corrections	36
4.5	Summary of Uncertainties	37
5	Proposed Run Plan	38
5.1	Tests and Milestones	38
5.2	Production Running	39
5.3	Beam Time Request	39
6	Summary	40
A	Intensity Feedback at the Polarized Source	40
A.1	Existing Polarized Electron Source (PES)	40
A.2	PES Modifications	42
A.3	Intensity Feedback Algorithm	44
B	Calibration of Sensitivity to Beam Parameters	44
C	Estimates of Physics Backgrounds	45
C.1	General Formalism	47
C.2	Inelastic Scattering from the Proton	47
C.3	Electroproduction of the Delta from Radiated Electrons	48
C.4	Electroproduction of Other Resonances from Radiated Electrons	49
C.5	Deep Inelastic Scattering	49
C.6	Pion Production by Real and Virtual Photons	51
C.7	Comments	52
D	Resources	53

List of Figures

1	Neutral current amplitudes leading to the asymmetry A_{LR} at tree level. . . .	9
2	The behavior of the asymmetry, the differential cross-section and the figure of merit (f.o.m.) as a function of $ \cos \Theta $, the scattering angle in the center of mass frame.	10
3	Dominant electroweak corrections to A_{LR} are shown, namely: $\gamma - Z$ mixing diagrams (a-b) and W -loop contribution to the anapole moment (c).	11
4	Selected measurements of $\sin^2 \theta_W$ as a function of Q^2 . The dashed line is the theoretical prediction at high Q^2 while the dotted line is the prediction at low Q^2	11
5	Schematic of main components of the liquid Hydrogen Target	19
6	Three views of the target loop	20
7	Schematic of the Spectrometer and Detector Layout in End Station A. Note the vastly different X and Z scales. Approximate horizontal ray traces of a few select electron trajectories are also shown.	22
8	Estimated beam profile in ESA, including multiple scattering in the target (at $z = 0$), as a function of distance, with (solid line) and without (dashed line) the effect of the spectrometer quadrupoles.	24
9	The distribution of electrons from Møller scattering (points) and e-p scattering (histogram) for 10^7 incident 48.3 GeV electrons, as a function of distance from the beam axis (left). On the right, the momentum distribution of electrons for $16.75 < r < 26$ cm.	25
10	Schematic of a Tungsten-Quartz fiber Calorimeter	27
11	Front and side view of the complete electron calorimeter	28
12	Arrangement of Plates and Fibers	28
13	Diagram of DAQ System	29
14	SLAC Polarized Electron Source	41
15	Polarized Electron Source for this Experiment	43

List of Tables

1	Previous Electroweak Measurements in Fixed Target \vec{e} Scattering	8
2	The discovery reach of various experiments to electron contact interactions. . .	13
3	The sensitivity of various experiments to the X parameter.	15
4	End Station A Beam Characteristics	17
5	Liquid Hydrogen Target Specifications	18
6	Acceptable beam parameter uncertainties per pulse (Column II) and their impact on $\delta(A_{LR})$ per pulse (Column III). Column IV shows the intrinsic pulse to pulse fluctuations for various beam parameters. The last column lists the maximum acceptable cumulative helicity correlated asymmetries for $\delta(A_{LR})_{\text{syst}} \leq 1 \times 10^{-9}$ from each parameter.	32
7	Summary Table of Physics Background Estimates	36
8	Estimated statistical error for a 20 week production run at 43% efficiency . .	37
9	Error Contributions to the Raw Asymmetry in Parts per Billion	38
10	Normalization Error Contributions to the Measurement of $\sin^2 \hat{\theta}_W(0)$	38
11	Summary of Beam Time Request	39
12	Beam Parameters for recent SLAC experiments	42
13	Beam Charge Asymmetry Beam Parameters	45

1 Introduction

Over the past decade, experiments measuring weak neutral current interactions have taken the lead in the study of electroweak radiative corrections, providing the best indirect probes of new high energy physics. Experiments on the Z^0 resonance have measured neutral current observables with spectacular precision, as evidenced by a precise indirect measurement of the mass of the top quark, which is in agreement with the direct measurement at the Tevatron.

At low Q^2 on the other hand, tests of the electroweak theory in the weak neutral current sector are typically less sensitive by more than an order of magnitude. A comprehensive search for physics beyond the standard model is incomplete unless equally sensitive measurements are carried out both on and off the Z^0 resonance. In this proposal, we describe a precision measurement of a low energy weak neutral current amplitude by the study of the spin dependence of polarized electron scattering off unpolarized electrons in an unpolarized target.

We propose a precision measurement of the left-right asymmetry (A_{LR}) in Møller scattering ($e^-e^- \rightarrow e^-e^-$), using the 48 GeV polarized electron beam in End Station A (ESA) at SLAC scattering off unpolarized electrons in a liquid hydrogen target, corresponding to an average Q^2 of 0.03 (GeV/c)^2 . The parity nonconserving piece of the electroweak interaction governing the Møller scattering process has never been measured before.

In the following sections, we describe an experimental design which would allow the measurement of the effective weak neutral current coupling governing low energy Møller scattering with a relative cumulative accuracy of 7% in a 5 month run, corresponding to a measurement of the weak mixing angle $\delta(\sin^2 \theta_W)_{\text{stat+syst}} \sim 0.0008$. This would test the electroweak theory at the quantum loop level for $Q^2 \ll M_Z^2$ for the first time and provide unique sensitivity to new physics at the TeV scale. It allows the exploration of electron compositeness scales better than 10 TeV, which achieves the same level of sensitivity as that accessed by LEP-II, the highest energy e^+e^- collider currently in operation.

The experiment would constitute the first time that a purely leptonic weak neutral current coupling is measured away from the Z^0 pole with sufficient precision to access electroweak radiative corrections. Such a measurement would set a new standard for precision electroweak measurements at low Q^2 .

2 Physics Motivation

2.1 Parity Violating Electron Scattering

Polarized electrons scattering off unpolarized targets provide a clean window to study weak neutral current interactions. These experiments measure an asymmetry defined by

$$A_{\text{LR}} = \frac{\sigma_R - \sigma_L}{\sigma_L + \sigma_L} \quad (1)$$

where σ_R (σ_L) is the scattering cross section using incident right (left) handed electrons. A non-zero asymmetry constitutes parity nonconservation and signals the presence of pseudo-scalar terms in the cross-section. For $Q^2 \ll M_Z^2$, A_{LR} is proportional to the ratio of these amplitudes and is about 10^{-4} for $Q^2 \sim 1(\text{GeV}/c)^2$ [1].

The SLAC measurement of parity violation in deep inelastic scattering off nucleons performed in 1978-79[2] was the first to devise experimental techniques required to measure such small asymmetries. Since that pioneering effort, the statistical and systematic precision achievable in the raw asymmetry in low Q^2 polarized electron scattering has improved steadily. The three published measurements which have measured electroweak asymmetries in low Q^2 electron scattering are tabulated in Table 1. Techniques have now been established to measure asymmetries with systematic errors less than 10^{-8} .

Laboratory	Q^2 (GeV/c) ²	Target	A_{LR} (ppm)	$\delta(A_{\text{LR}})$ (ppm)
SLAC[2]	1.6	D ₂	150	±15
Mainz[3]	0.3	⁹ Be	3.7	±0.7 ± 0.2
Bates[4]	0.02	¹² C	0.7	±0.14 ± 0.02

Table 1: Previous Electroweak Measurements in Fixed Target \vec{e} Scattering

Attempts to design new experiments with higher precision in the weak neutral current couplings have been limited by theoretical uncertainties. In elastic scattering, the important theoretical uncertainties arise from the lack of knowledge of strange quark form factors, whereas in deep inelastic scattering, theoretical uncertainties originate from strange sea quark distributions and the magnitude of higher twist effects[5]. In this proposal, we consider the Møller scattering of polarized electrons off atomic electrons, a purely leptonic reaction which is calculable to a high accuracy in the electroweak theory.

2.2 Left-Right Asymmetry in Møller Scattering

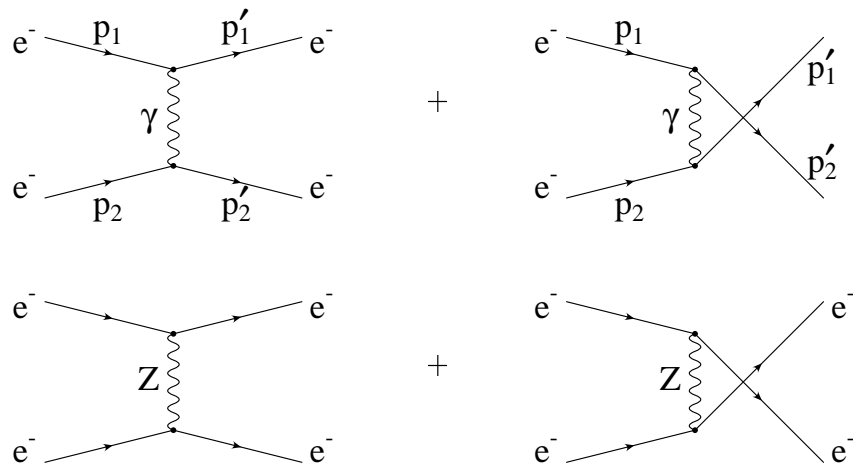


Figure 1: Neutral current amplitudes leading to the asymmetry A_{LR} at tree level.

The leading order Feynman diagrams relevant for Møller scattering are shown in Fig. 1. The spin averaged differential cross section is given by

$$\frac{d\sigma}{d\Omega} = \frac{\alpha^2}{2mE} \frac{(3 + \cos^2 \Theta)^2}{\sin^4 \Theta} \quad (2)$$

where α is the fine structure constant, E is the incident beam energy, m is the electron mass and Θ is the scattering angle in the center of mass frame. Its behaviour as function of $\cos \Theta$ (Eqn. 2) is shown in Fig. 2a.

The parity-violating asymmetry A_{LR} , due to the interference between the weak and electromagnetic diagrams in Fig. 1, is given by[6]

$$A_{LR} = mE \frac{G_F}{\sqrt{2}\pi\alpha} \frac{16 \sin^2 \Theta}{(3 + \cos^2 \Theta)^2} g_{ee}. \quad (3)$$

where G_F is the Fermi coupling constant and g_{ee} is the pseudo-scalar weak neutral current coupling governing Møller scattering. At tree level in the standard model one has:

$$g_{ee} \equiv \rho \cdot g_{Ve} \cdot g_{Ae} = \frac{1}{4} - \sin^2 \theta_W. \quad (4)$$

For $E = 50$ GeV, $E' = 25$ GeV and 100% beam polarization, A_{LR} is 3.2×10^{-7} . Radiative corrections reduce this asymmetry by more than 40%[7], as discussed in Sec. 2.3.

As shown in Fig. 2a, the asymmetry (Eqn. 3) is maximal at $E' = 25$ GeV ($\cos \Theta = 0$) and falls to zero at $E' = 0$ and 50 GeV. For the experimental design, an important parameter is the figure of merit (f.o.m.), which quantifies the variation of the achievable statistical error

for fixed luminosity. It can be seen in Fig 2b that the f.o.m. varies slowly with $\cos \Theta$ and is maximal at $E' = 25$ GeV. Our spectrometer has been designed to accept scattered electrons in the range $-0.5 < \cos \Theta < 0$ in the full range of the azimuth, providing a total cross section of about $14 \mu\text{Barns}$.

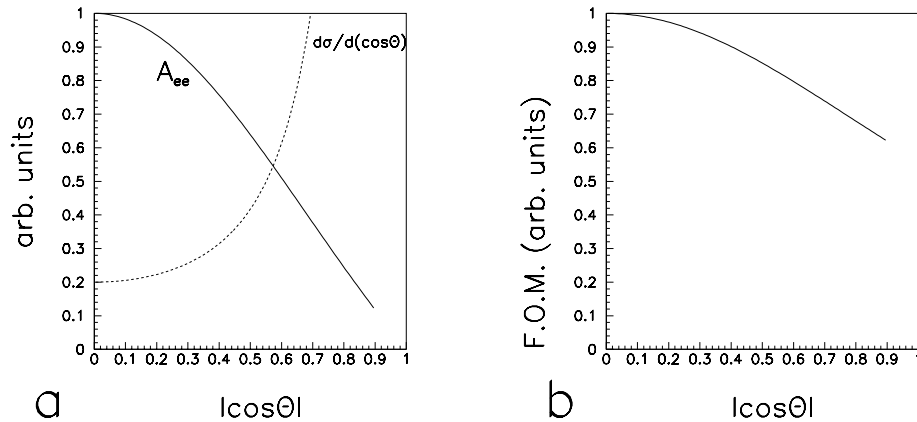


Figure 2: The behavior of the asymmetry, the differential cross-section and the figure of merit (f.o.m.) as a function of $|\cos \Theta|$, the scattering angle in the center of mass frame.

With a 10 gm/cm^2 liquid hydrogen target and a beam current of $8\text{-}12 \mu\text{A}$, it is thus possible to achieve a fractional statistical error of 6% on the experimental asymmetry in a 20 week production run at 43% efficiency[†]. This measures $\sin^2 \hat{\theta}_W(0)$ with a precision of 0.0007, since the asymmetry is proportional to $(1 - 4 \sin^2 \theta_W)$:

$$g_{ee} \equiv \frac{1}{4} - \sin^2 \hat{\theta}_W(0) \implies \frac{\delta(\sin^2 \hat{\theta}_W(0))}{\sin^2 \hat{\theta}_W(0)} \simeq 0.05 \frac{\delta g_{ee}}{g_{ee}}. \quad (5)$$

The proximity of the value of $\sin^2 \hat{\theta}_W(0)$ to 0.25 thus alleviates the impact of normalization errors such as the estimation of the electron beam polarization. For electrons from a hydrogen target, the relevant backgrounds are elastic and inelastic electron proton scattering and photoproduction of pions off protons at very low Q^2 , which are well understood, and can be suppressed (see Appendix C).

[†]The experiment is assumed to run parasitic with PEP-II. The efficiency has been estimated taking into account the overhead in switching the beam every hour between PEP-II and ESA.[8]

2.3 Standard Model Radiative Corrections

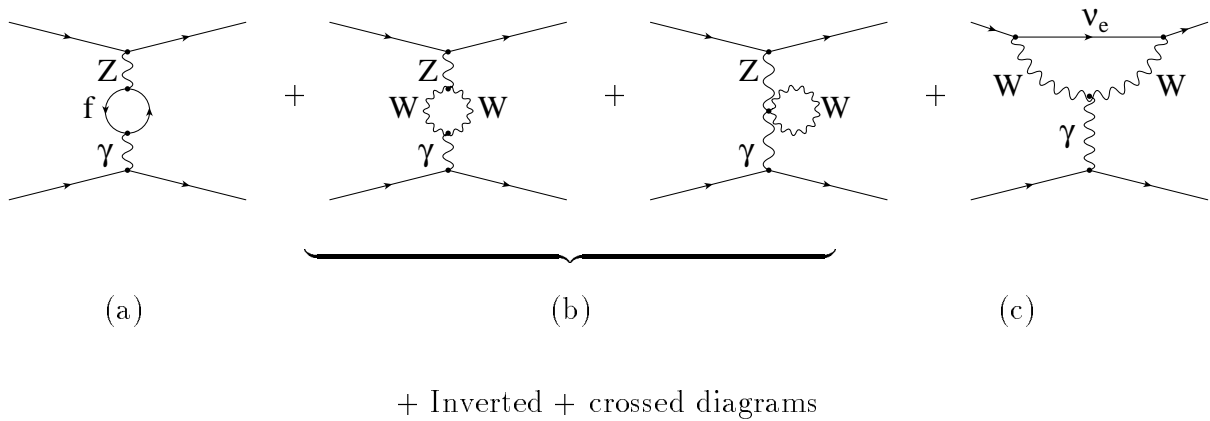


Figure 3: Dominant electroweak corrections to A_{LR} are shown, namely: $\gamma - Z$ mixing diagrams (a-b) and W -loop contribution to the anapole moment (c).

The one loop electroweak radiative corrections to A_{LR} have been estimated by Czarnecki and Marciano[7]. The most important loop corrections come from the $\gamma - Z$ mixing and the anapole moment diagrams illustrated in Fig. 3. The overall correction from the above mentioned diagrams produces a 38% reduction in the tree level prediction of A_{LR} .

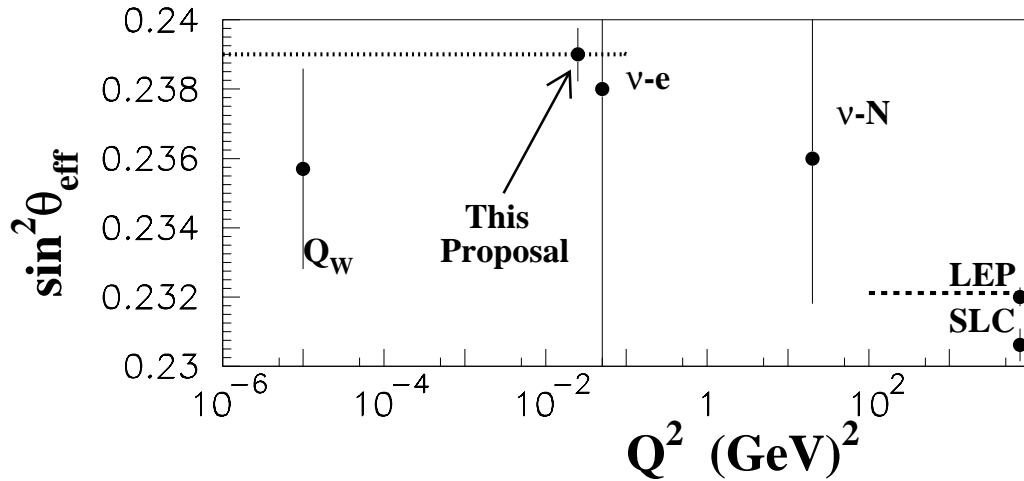


Figure 4: Selected measurements of $\sin^2 \theta_W$ as a function of Q^2 . The dashed line is the theoretical prediction at high Q^2 while the dotted line is the prediction at low Q^2 .

The projected experimental measurement would establish the running of $\sin^2 \theta_W$ at the 8σ level. Currently, this running has been established with marginal significance, $\sim 2\sigma$, as

shown in Fig. 4 with values derived from a compilation for a recent global analysis[9]. The impact of the Møller asymmetry measurement on establishing this remarkable prediction of the standard model is also shown. The level of sensitivity serves to underscore the sensitivity of the measurement to new tree level and loop level physics beyond the standard model.

2.4 New Physics Sensitivity

As discussed above, the measurement would test the electroweak theory at the loop level, away from the Z^0 resonance for the first time. The measurements at different energy scales, when taken together, can reveal the existence of new interactions or substructure. It is also possible to explore the effects of new physics that is manifest at the loop level.

2.4.1 New Neutral Gauge Bosons

Many extensions of the standard model predict new interactions at the TeV scale. If the interaction is mediated by a new neutral gauge boson Z' which does not mix significantly with the Z^0 , it could have escaped detection in past experiments. The proposed measurement is sensitive to parity violating weak neutral current interactions involving left and right handed electron currents of the form:

$$\sigma_L - \sigma_R \propto (\bar{\psi}_L \gamma^\mu \psi_L)^2 - (\bar{\psi}_R \gamma^\mu \psi_R)^2 \implies \delta(A_{LR}) \propto \frac{e^2(Q_L^2 - Q_R^2)}{M_{Z'}^2}, \quad (6)$$

where $\psi_{R,L}$ and $\bar{\psi}_{R,L}$ are electron chiral spinors and eQ_L and eQ_R are the chiral couplings of the electron to the Z' boson.

One can quantify the sensitivity of the measurement to a new interaction by evaluating the Z' mass $M_{Z'}$ for which the experimental measurement differs from the theoretical prediction by 2 standard deviations. For the proposed measurement, one obtains:

$$M_{Z'}^2 = (1.0 \text{ TeV})^2(Q_L^2 - Q_R^2). \quad (7)$$

The squared difference of the couplings could be as large as 1.4, giving rise to a sensitivity that exceeds 1 TeV.

The sensitivity ranges from 600 to 900 GeV for the Z' mass in specific models, similar to that expected with one or two years of data in the next running cycle of the Tevatron[10]. There are two important reasons why an indirect search for new neutral gauge bosons is a necessary complement to direct searches in high energy colliders. Firstly, the sign of the shift

relative to the standard model prediction indicates whether left or right handed electrons couple more strongly to the Z' boson. Secondly, the sensitivity of A_{LR} to new bosons is very model dependent. This would be very useful in discriminating between models, should a new gauge boson be observed in a high energy experiment.

2.4.2 Other Contact Interactions

Sensitivity to contact interactions is quantified by the mass scale at which new unknown dynamics become important. Considering only helicity and flavor conserving interactions, the general four-electron contact interaction Lagrangian takes the form[11]

$$\mathcal{L}_{ee} = \frac{4\pi}{2\Lambda_{ee}^2} \left[\eta_{LL}(\bar{\psi}_L\gamma_\mu\psi_L)^2 + \eta_{RR}(\bar{\psi}_R\gamma_\mu\psi_R)^2 + 2\eta_{LR}(\bar{\psi}_R\gamma_\mu\psi_R)(\bar{\psi}_L\gamma_\mu\psi_L) \right] \quad (8)$$

where Λ_{ee} is the compositeness scale for contact interactions among electrons.

Current limits on Λ_{ee} from e^+e^- colliders are in the range of 1 to 3 TeV[12]. The high statistics data accumulated on the Z^0 resonance has had little impact on these limits. Since the contact interaction amplitude is real, it does not interfere with the purely imaginary Z^0 amplitude at the pole. Therefore, the sensitivity to contact interaction terms in the Z^0 data is highly suppressed. The proposed measurement has high sensitivity to new contact interactions, provided there are parity violating terms:

$$g_{ee}(\text{meas.}) - g_{ee}(\text{theory}) = \pm \frac{\pi}{G_F\sqrt{2}} \frac{(\eta_{RR} - \eta_{LL})}{\Lambda_{ee}^2}. \quad (9)$$

The sensitivity is compared with other relevant processes in Table 2.

2 σ limits on Λ_{ee} (TeV)	
Experiment	η_{RR} or $\eta_{LL} = \pm 1$
PEP/PETRA[12]	1.5
ALEPH[16]	1.8
$\delta(A_{LR})/A_{LR} = 1\%$ at SLD	~ 4.0
LEP-II ($\sqrt{s} = 170$ GeV, 500 pb $^{-1}$)	~ 4.0
This Proposal	11.1

Table 2: The discovery reach of various experiments to electron contact interactions.

An example of a new four-electron contact interaction is that mediated by a doubly charged Higgs boson Δ^{++} which abound in exotic Higgs representations and appear in many

models[13]. Limits up to 45 GeV down to very small couplings exist from Z^0 resonance experiments[14]. If the scale of the interaction is much smaller than the mass of the Higgs boson M_Δ , the interaction Hamiltonian can be cast in the form of Eqn. 8[15]:

$$\frac{g_{ee\Delta}^2}{M_\Delta^2} = \frac{4\pi}{\Lambda_{ee}^2} \eta_{RR}, \quad (10)$$

where $g_{ee\Delta}$ is the $ee\Delta$ coupling. Indirect constraints from $(g-2)_\mu$, muonium-antimuonium conversion and exotic muon decay are typically at the level of $g_{\ell\ell\Delta}^2/M_\Delta^2 \leq 10^{-6} \text{ GeV}^{-2}$. For the Møller A_{LR} measurement, $\Lambda_{ee} = 10 \text{ TeV}$ corresponds to $g_{ee\Delta}^2/M_\Delta^2 \sim 10^{-7} \text{ GeV}^{-2}$, an improvement of an order of magnitude.

2.4.3 Oblique Corrections

Since the standard model is a renormalizable quantum field theory, it is possible to make accurate predictions for experimental observables including higher order corrections. At the loop level, particles that are much heavier than the energy scale of the experiment can contribute to the corrections. Moreover, due to the fact that the electroweak gauge symmetry is spontaneously broken, these effects do not vanish even if the Q^2 of the experiment becomes much smaller than the scale of the relevant high energy physics.

One important class of virtual effects consists of the oblique quantum corrections[17], where new physics at a heavy mass scale can modify the effective couplings of low energy electroweak processes via quantum loops in the W and Z propagators[18]. If the new physics scale is large compared to the gauge boson masses, it can be shown[20] that only three new parameters need to be introduced, called S , T and U in one parameterization.

It turns out that only S and T affect Z^0 pole observables[19, 20] and are hence now significantly constrained by Z^0 resonance measurements. However, if the new physics scale is close to the masses of the weak vector bosons, more parameters must be introduced. It has been shown that[21, 22] only three more parameters need to be introduced, called V , W and X in one parameterization. On the Z^0 resonance, all constraints are valid as long as the parameters S and T are replaced by new expressions. They are listed below, along with current values from a global fit:[23]

$$S' = S + 4s^2c^2V + 4(c^2 - s^2)X = -0.33 \pm 0.19 \quad (11)$$

$$T' = T + V = -0.17 \pm 0.21. \quad (12)$$

Here, s^2 and c^2 denote $\sin^2 \theta_W$ and $\cos^2 \theta_W$ respectively. Hence, to obtain constraints on all parameters independently, additional measurements must be obtained at energy scales away from the Z^0 resonance.

The parameter X is simply a measure of the running of $\sin^2 \theta_W$. While the exact expression is renormalization scheme dependent, to a good approximation one can write:

$$\sin^2 \hat{\theta}_W(M_Z^2) - \sin^2 \hat{\theta}_W(0) \simeq \alpha X, \quad (13)$$

where α is the fine structure constant. The current world average is $X = 0.38 \pm 0.51$ [23]. We compare this sensitivity to other potential measurements of the X parameter in Table 3. It should be emphasized that the nature of the radiative corrections that are described by the three new parameters are different in character from S , T and U . A nonzero value of X would indicate that the new physics scale is not much higher than the electroweak scale, and that the new physics does not couple strongly to the Z^0 boson.

Current World Average $\delta(X) = 0.51$		
Experiment	process	$\delta(X)$
Atomic Parity	e-q	0.4
ν -N DIS (NuTeV)	ν -q	0.4
This Proposal	e-e	0.1

Table 3: The sensitivity of various experiments to the X parameter.

3 Experimental Design

The polarized source generates pulses of electrons at 120 Hz with the ability to assign the sign of the beam polarization on a pulse to pulse basis. The experimental asymmetry is measured by rapidly flipping between the two possible electron beam helicity states while keeping all other experimental parameters virtually unchanged and then averaging the fractional difference in the cross-section over many such complementary pairs of pulses. The most important design requirement is a very high event rate. In our design, between 2×10^7 and 4×10^7 electrons will be detected every beam pulse.

At this high rate, integrating the signal over the duration of the beam pulse is most practical, eliminating dangerous dead time problems. The integration technique requires

that elastically scattered electrons be focused into a region otherwise free of background into total absorption shower counters. This is possible with a modest spectrometer system, primarily due to the fact that the nominal Q is just above the pion mass. Therefore, the non-electron background is expected to be small, and the light output of the absorption counters should be completely dominated by the Møller electron showers. The spectrometer is designed to accept Møller electrons in the momentum range 12 to 24 GeV/c.

An ideal source of target electrons is a liquid hydrogen target. The total cross section over the range of spectrometer acceptance is $14\mu\text{barns}$. In order to achieve the necessary rate, one needs 10 gm/cm^2 of liquid Hydrogen, which is about 150 cm long, which in turn requires a cryogenic target system capable of handling a load of 600 W from the beam.

The electron beam polarization will be measured by periodically replacing the hydrogen target with a polarized iron foil, and measuring the resulting asymmetry in the scattering of the polarized beam electrons off of polarized target electrons. Thus, the same apparatus and measuring technique will be used to measure the expected QED asymmetry as that used to measure the electroweak asymmetry.

The primary responsibilities of the participating institutions in the design and construction of the experimental apparatus are tabulated in Appendix D. In the following, we summarize the most important aspects of the experimental design.

3.1 Polarized Beam

3.1.1 Electron Source

Polarized electrons are produced by photoemission from a GaAs photocathode. For fixed target experiments at SLAC, a flash lamp pumped Ti:sapphire laser is used to produce one 100-350 ns pulse. The laser light is polarized by two Pockels cells. The changes to the polarized source optics configuration for this proposal are described in Appendix A. The most important new requirement is the stringent control of helicity correlations in the laser light impinging on the photocathode. Most of the helicity correlations in the electron beam can be traced back to helicity correlations in the physical characteristics of the laser light. A description of the effects and our strategy to reduce helicity correlations are discussed in Sec. 4.1.1 and in detail in Appendix A.

3.1.2 Electron Beam in ESA

The polarized beam will be required to produce $(3 - 6) \times 10^{11}$ electrons per pulse with 80% beam polarization at a repetition rate of 120 Hz. In order to cancel systematic effects, the experiment will be carried out at two beam energies, 48.3 GeV and 45.0 GeV. At these energies, the electron beam polarization in the End Station is longitudinally polarized but the number of $g - 2$ precessions differs by 1/2, thus changing the sign of the measured experimental asymmetry. The statistical power of the asymmetry measurement increases linearly with increasing beam energy while the maximum available beam current reduces with increasing beam energy. We plan to run 60% of the time at 48 GeV, which would achieve equal statistical errors on the two oppositely signed raw asymmetries. The assumed beam requirements are summarized in Table 4.

Polarization	80%
Intensity at 48 GeV	3.5×10^{11} e ⁻ /pulse
Intensity at 45 GeV	6×10^{11} e ⁻ /pulse
Pulse Length	~100-350 ns
Repetition Rate	120 Hz
Beam Spot	~ 1 mm
Intensity Jitter per pulse	2%
Energy Jitter per pulse	0.4%

Table 4: End Station A Beam Characteristics

3.2 Liquid Hydrogen Target

3.2.1 Design Specifications

The most practical 'electron' target with a minimum radiation length per target electron is hydrogen. We propose to use a 1.5 meter long liquid hydrogen target, similar in design to the target used in a parity violation experiment called SAMPLE [24] at the MIT-Bates laboratory. Specifications for the proposed target are given in Table 5. The SLAC target will be longer than the Bates target, and will have more stringent requirements on the target window curvature and on possible allowable density fluctuations. The SLAC target however has a similar total power requirement, since the beam current at SLAC is significantly less

than that at Bates. As a result, we propose to use a design based closely on the existing Bates target. The Bates target has been subject to an extensive safety review; consequently it should be straightforward to satisfy the safety criteria at SLAC.

Refrigeration capacity	700 W
Operating temperature	20 K
Operating pressure	30 psia
Density	0.07 gm/cm ³
Target thickness	11 gm/cm ²
Length	1.5 meters
Flow rate	10 m/s
Liquid hydrogen	25 liters

Table 5: Liquid Hydrogen Target Specifications

The target will consist of liquid hydrogen flowing through a closed loop system. A schematic of the target is presented in Fig. 5 and a drawing of the loop is shown in Fig. 6.

The hydrogen will be cooled to 20° K using a counterflow heat exchanger flowing cold helium gas at 16 psia in a jacket outside the hydrogen target. The cold helium will be provided by an 800 Watt refrigeration system similar to that used in the Bates experiment. The hydrogen target will be housed inside a vacuum chamber attached to the electron beam line. Hydrogen will be admitted to the target through a gas control system which will contain safety relief valves to ensure that the target operation is safe for personnel and equipment. The operating parameters of the target will be monitored by a PC.

To summarize, the target will consist of the following systems: (1) a target cell, (2) a target loop, (3) a refrigeration system, (4) a gas handling system, (5) a control system. A short description of each is given below.

3.2.2 Major Systems

The target cell will be cylindrical, 3 inches in diameter and 150 cm long. The entrance and exit windows will have the same radius of curvature to ensure that the liquid hydrogen target thickness is independent of the position of the incident electron beam. A separate helium cell will be used to maintain a constant pressure on the concave entrance window.

The target loop consists of a heat exchanger, pump, target cell and manifold. It will

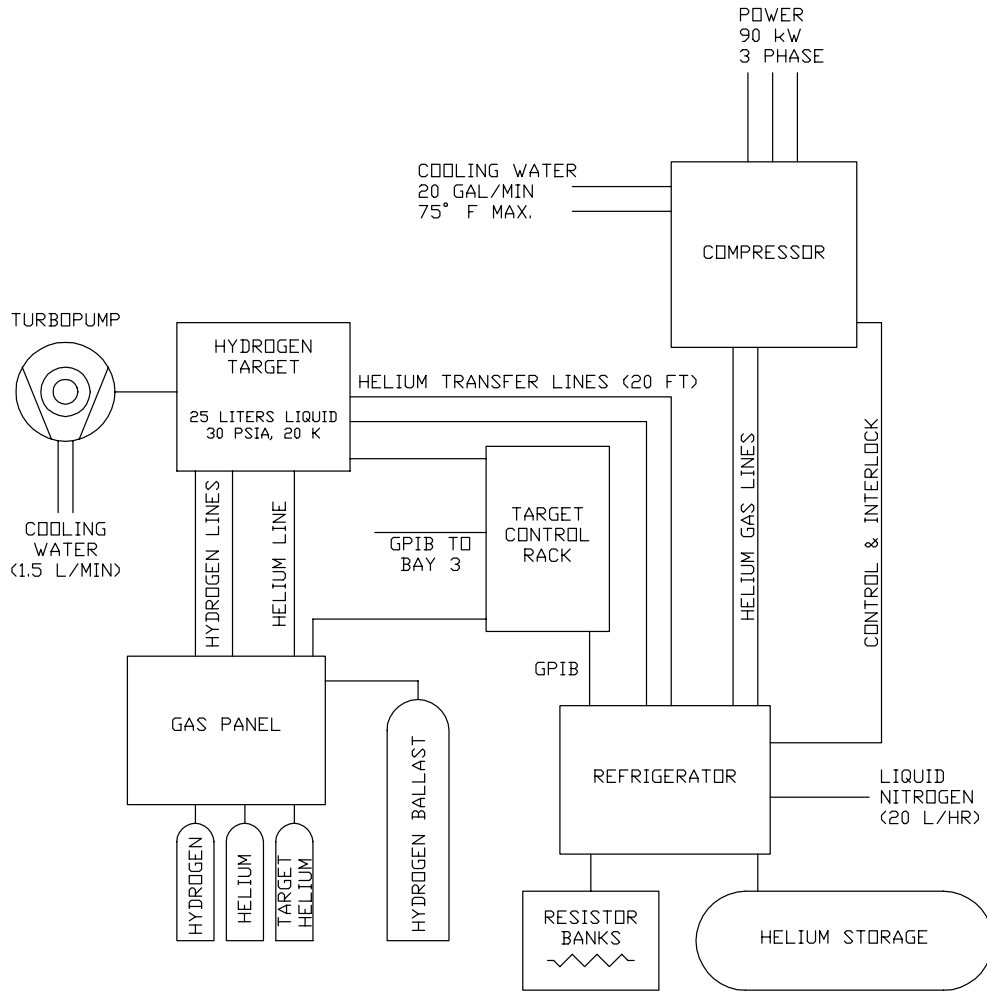


Figure 5: Schematic of main components of the liquid Hydrogen Target

contain a total of about 25 liters of liquid hydrogen. The pump establishes the flow of hydrogen throughout the loop. The heat exchanger will consist of a copper hose inside a stainless steel pipe. As hydrogen flows through the copper hose, helium will flow in the opposite direction between the copper and stainless steel pipe. A heater within the target loop will be used to maintain the hydrogen temperature if there is a change in beam power in the target. The heater will be controlled by a feedback loop with the electron beam current. The required refrigeration system will be similar to that used at SAMPLE[‡].

Target control will be handled by a PC which will monitor the state of the gas handling system and record the temperature and pressure of the target hydrogen and helium at several locations. Stepping motors will be used to move the target transverse to the beam

[‡]Process Systems International model 1620-S refrigeration system

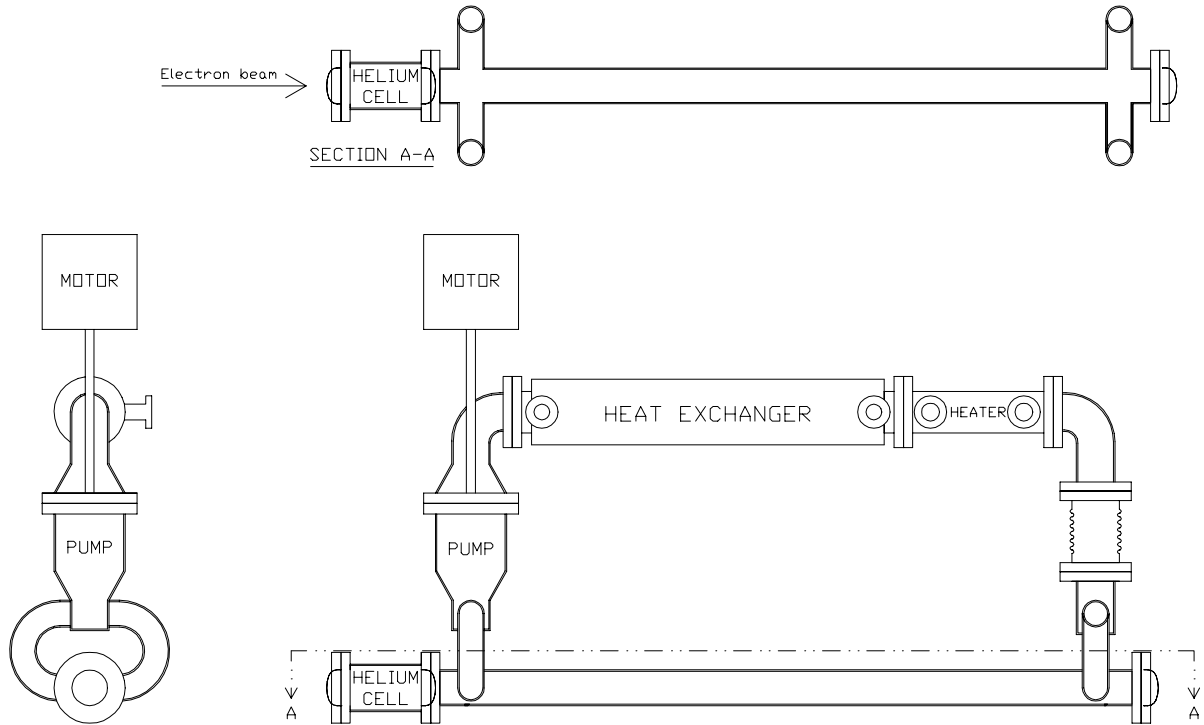


Figure 6: Three views of the target loop

spot position.

Density fluctuations in the Møller target must be maintained to better than 10^{-4} on a pulse to pulse basis. If not, the statistical error for a given luminosity would increase. At present, the SAMPLE experiment has determined that with a $40\mu\text{Amp}$ beam current on a 40 cm cell, the target experiences less than 0.1% density fluctuations. For the Møller target, we plan to monitor and study the luminosity on the target using a low scattering angle detector to search for density fluctuations. For $\theta_{\text{lab}} \sim 1$ mrad, the asymmetry in the spin-dependent e-p scattering cross-section is negligible compared to even the Møller electroweak asymmetry. As a result, the low angle detector can be used to measure a zero of the asymmetry (a powerful calibration tool) and to monitor and measure the size of density fluctuations.

3.3 The Spectrometer

3.3.1 Design Criteria

The salient features of the spectrometer system are:

- Full azimuthal acceptance for Møller scattered electrons with momentum in the range 12-24 GeV/c.
- Clean separation between the Møller electrons, the e-p radiative tail and the bremsstrahlung degraded primary beam, exploiting the energy angle correlation of Møller electrons.
- Placement of the detectors out of the line-of-sight of the target.
- Direction of the large flux of bremsstrahlung photons and the primary beam to the ESA beam dump, thus minimizing backgrounds.
- Further reduction of the target photon background by proper arrangement of collimators resulting in a "two bounce" photon system.
- Separation of the substantial flux of positrons and their elimination by subsequent collimation.
- Provision of adequate clearance for the primary beam at the 10σ or more level throughout the beam pipe and collimators, thereby providing adequate space to shield detectors from ambient backgrounds.
- Minimization of costs by the use of existing magnets.

3.3.2 ESA Layout

The layout in End Station A of the spectrometer system that can best satisfy the above criteria is shown in Fig 7. It consists of three dipole magnets in a "chicane" D $\bar{D}\bar{D}$ configuration followed by four quadrupole magnets. The primary beam as well as the Møller electrons travel cleanly through all seven magnetic elements.

All magnets come from the End Station A spectrometer facilities (8 GeV/c and 20 GeV/c spectrometers). The two outer elements of the chicane are the 12D125 dipoles (B202 and B204) from the 20 GeV/c spectrometer. The middle chicane element is one of the 22D136 dipoles of the 8 GeV/c spectrometer (B81). All three magnets are of the highest quality iron dominated dipoles ever built. The four quadrupoles are 15Q51 elements from the 8 GeV/c (Q82 and Q83) and the 20 GeV/c spectrometer (Q202 and Q203). They are among the most

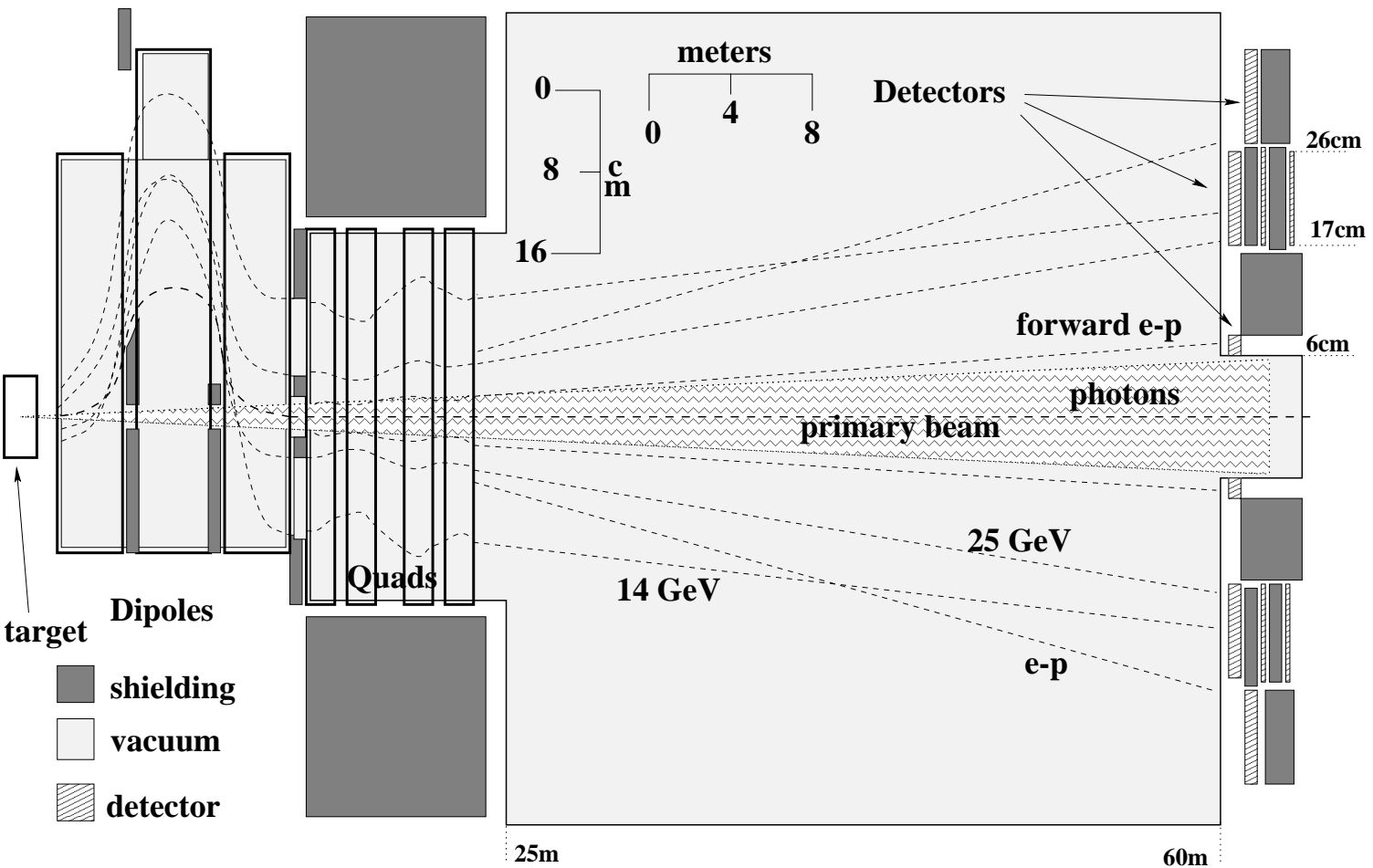


Figure 7: Schematic of the Spectrometer and Detector Layout in End Station A. Note the vastly different X and Z scales. Approximate horizontal ray traces of a few select electron trajectories are also shown.

uniform iron dominated quadrupoles available today with a gradient variation of less than 1% over a 19.4 cm radius.

The main purpose of the chicane is to put the detector out of the line-of-sight of the target and to create a “two bounce system” for most of the photons with the help of strategically placed collimators. Photons originating from radiative processes in the target can reach the detector only after bouncing twice on the vacuum pipe apertures or collimators. A similar strategy was employed successfully in the small angle/large acceptance E142/3 [25] and E154/155 spectrometers [26].

The first order optics matrix of the chicane is equivalent to that of a drift length in both horizontal and vertical directions, since the chicane is designed to operate as an achromat. The purpose of the quadrupoles is to focus the Møller scattered electrons of interest (electrons with scattering angles in the range $\theta=4.5-7.2$ mr) in a concentrated detector area resulting in a minimal contamination from electrons from radiative scattering off target protons.

3.3.3 Primary Beam Profile and Containment

The proximity of the detectors to the beam line requires a beam tune that results in the smallest beam spread possible at the end of ESA where the detectors will be located. The beam spot size depends on a) the optics of the A-Line (tuning of its quadrupoles), b) the multiple scattering introduced by the longitudinal extent of the hydrogen target, and c) the overall focusing by the Møller spectrometer quadrupoles.

Since the multiple scattering spread is fixed, we have tuned the A-Line quadrupoles so that the beam spread at the end of ESA is not dominated by the A-Line optics but rather by the target multiple scattering. At the same time, the beam spot at the target is of the order $\sigma_x \simeq \sigma_y \simeq 1$ mm like in previous ESA experiments. The expected beam size at the detector area is $\sigma_x \simeq \sigma_y \simeq 5$ mm. Figure 8 shows the estimated beam envelope in both dimensions, with and without the focusing effect of the spectrometer quadrupoles. The Møller calorimeter shielding and the luminosity monitor will be at a comfortable 12σ , in both x and y , away from the beam axis.

The unusual nature of the spectrometer, with its redirection of the primary beam, and the high current in the End Station will require additional precautions to conform to safety requirements. A preliminary study for beam containment has been carried out. The dipoles of the chicane will be instrumented with meter relays so that the beam is turned off when the

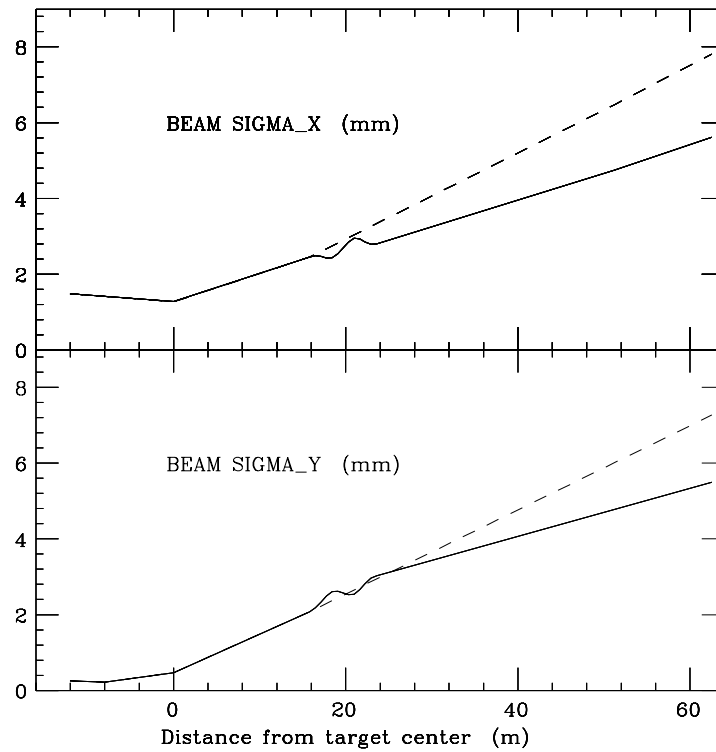


Figure 8: Estimated beam profile in ESA, including multiple scattering in the target (at $z = 0$), as a function of distance, with (solid line) and without (dashed line) the effect of the spectrometer quadrupoles.

current in the dipole magnets deviate substantially from their nominal values. Based on a ray trace study, burn through monitors (BTMs) will be installed downstream of the quadrupoles as well as downstream of the detectors at regions corresponding to the maximum possible deviation of the primary beam. A toroid comparator will be placed around the beam axis downstream of the detectors which will be set so that the maximum possible fraction of primary beam lost in ESA is limited to 20%.

3.3.4 Simulation Results

We have carried out an investigation of the spectrometer design using a GEANT[27] Monte Carlo simulation of 10^7 48.3 GeV electrons traversing a 1.5 meter hydrogen target. A complete treatment of multiple and single coulomb scattering, energy loss fluctuations and bremsstrahlung were included. Above a threshold of 10 MeV, discrete δ -ray and bremsstrahlung interactions were simulated. Compton scattering and pair production from the bremsstrahlung photons were included.

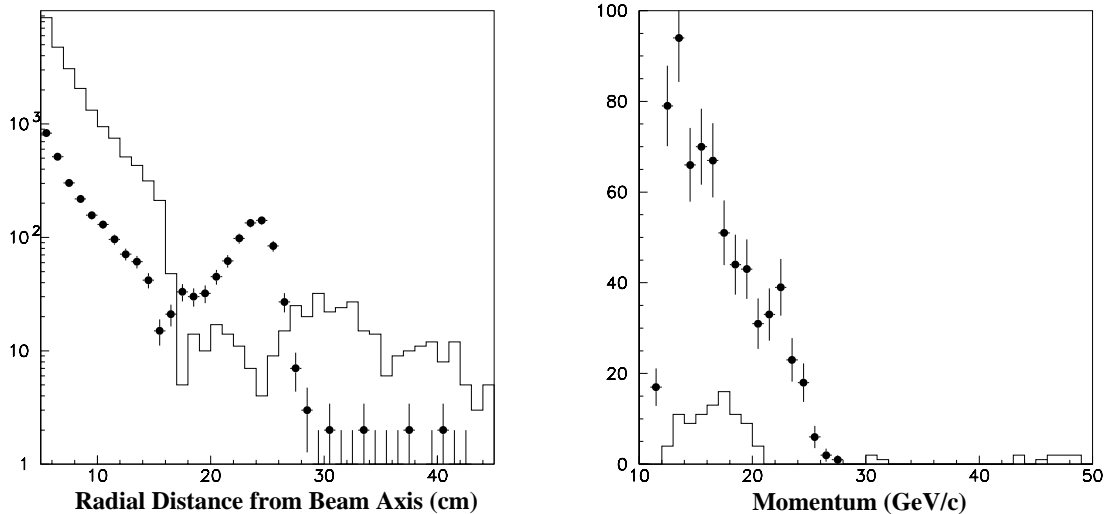


Figure 9: The distribution of electrons from Møller scattering (points) and e-p scattering (histogram) for 10^7 incident 48.3 GeV electrons, as a function of distance from the beam axis (left). On the right, the momentum distribution of electrons for $16.75 < r < 26$ cm.

Figure 9 shows the distribution of Møller electrons and e-p electrons as a function of the distance from the beam axis. It can be seen that the Møller signal dominates in the region between 16.5 and 26 cm, where the Møller calorimeter will be placed. The region between 28 cm and 40 cm from the beam axis is dominated by e-p electrons from the same laboratory scattering angles as the signal Møller electrons, and will be used to estimate the background e-p asymmetry. The region between 6 and 8 cm has a large signal from e-p scattering and will be used to monitor pulse to pulse luminosity fluctuations and false asymmetries.

Figure 9 also shows the distribution of Møller electrons and e-p electrons as a function of momentum in the region to be covered by the Møller calorimeter. The signal is 690 events for 10^7 incident electrons, corresponding to about 85% of the Born cross section. The e-p background is $13 \pm 1\%$ of the total rate into the detector.

3.4 Calorimeter

The main focus of this section will be the Møller electron calorimeter, which will be the primary detector. In addition, we will add a similar “ep electron calorimeter” and a “pion” calorimeter to monitor the asymmetries of background processes. The design is driven mainly by the need to integrate the calorimeter response to determine the scattered flux over the duration of the beam pulse, in a high radiation environment.

3.4.1 Basic Specifications

We have produced an economical design for the calorimeter that will meet the following special needs of our experiment:

- Maximal response to electrons.
- Moderate resolution $\sigma_E/E \approx 0.1$ in the range from 10 to 25 GeV; negligible fluctuations due to phenomena such as the Landau tail.
- Small response from pions and negligible response from muons
- Small response from low energy photons and hadrons
- No response from nuclear breakup or heavy ions (nonrelativistic particles)
- Excellent radiation resistance.

One of the most severe requirements is the large radiation resistance. For a scattered electron rate of 3×10^7 electrons per pulse at 120 Hz for 10^7 seconds, the accumulated charge is about 6 mC. For an average electron energy of 17 GeV, this leads to a total deposited energy of 100 MJ. The Møller electrons will cover a cross sectional area of about 1000 cm². If 100 kg of detector material is used, the total dose over the duration of the experiment would be 1 MJ/kg or about 10 Mrad every 2 weeks. Therefore, convenient total absorption crystal calorimetry options such as lead glass or lead fluoride are ruled out.

In order to satisfy the above criteria, our first choice is a sampling calorimeter made up of alternate layers of quartz fibers[§](active medium) and tungsten (absorber). Such detectors have been tested as possibilities for very forward angle calorimeters at future colliders and are expected to withstand radiation doses exceeding 1 Grad[28].

Alternative choices include liquid or high pressure noble gas ionization detectors. However, considerations such as low energy neutron proton scattering, cryogenics and edge effects make these choices potentially more complicated. In the following, we describe the geometry of a quartz-tungsten detector. However, a detailed comparison of performance and cost with a realistic ionization detector will be made before proceeding further with detector design.

[§]The “quartz” fibers are made of amorphous silica

3.4.2 Detector Geometry

The basic design of a tungsten-quartz fiber calorimeter is given in Fig. 10. The detector is a sandwich of thin ~ 3 mm tungsten plates and layers of quartz fibers. The plates are oriented at 45° to the incident particles so that some of the Čerenkov radiation will be emitted in a direction parallel to the fibers. Once the fibers exit the tungsten, they are bent so that Čerenkov radiation from particles traversing parallel to the beam pipe outside the tungsten do not produce photons.

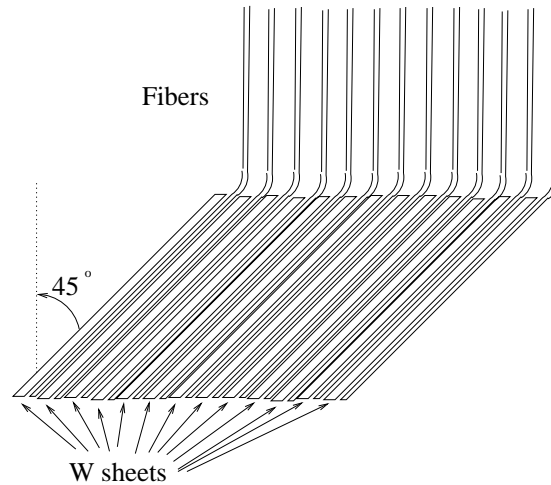


Figure 10: Schematic of a Tungsten-Quartz fiber Calorimeter

The calorimeter will have a cylindrical geometry centered about the beam line as shown in Fig. 11. The device will be divided into 8 identical octants which will be read out independently. This will provide information about any ϕ -dependence of the asymmetry. The fibers will cover the plate uniformly. A side view of a typical stack of plates is given in Fig. 12. The fibers will be tightly packed in each single layer so that sampling fluctuations from narrow showers are negligible.

3.4.3 Signal and Background Estimates

The calorimeter will be 15 radiation lengths (RL) in order to suppress minimum ionizing particles (MIPs). MIPs create a signal of 800 MeV in a 30 RL device[28], so it will be 400 MeV for our design, or 3% of the signal from a single electron. The short detector will also provide suppression of pion backgrounds. The average contribution from charged pions will be about 12% of the electron signal at 10 GeV. Since we anticipate a flux of pions of at most 1% of the electron flux, the total contribution to our signal will be 0.1%, a level that we can

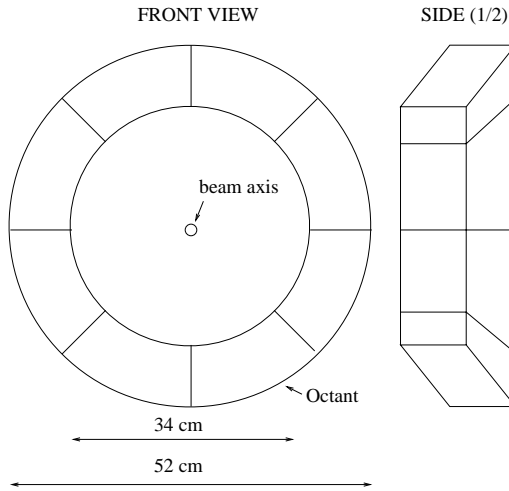


Figure 11: Front and side view of the complete electron calorimeter

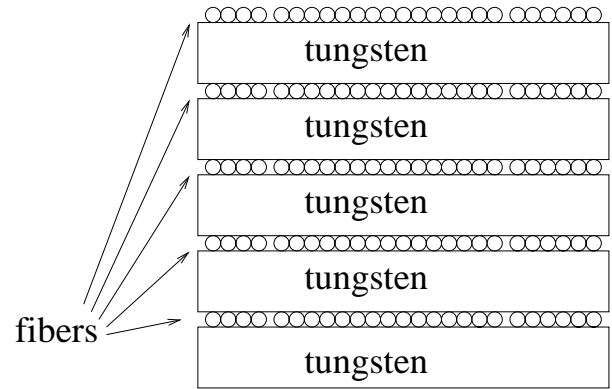


Figure 12: Arrangement of Plates and Fibers

tolerate comfortably. The 5% energy fluctuations due to the short length will cause a small degradation of the resolution.

Another source of background is electrons from elastic proton scattering. To monitor the asymmetry of these particles, a second electron calorimeter similar to the one just described will be added. It will have a larger radius so that it is in a region where there are no Møller electrons. Only about one quarter of the ϕ angle will need to be covered. We also plan to monitor the asymmetry of pions and muons that traverse the Møller electron calorimeter. This will be done by integrating the response of scintillators placed behind the electron calorimeter, after a few nuclear interaction lengths of absorber.

Finally, we plan to monitor elastic electron-proton scattering at very forward angles as a method to keep track of pulse to pulse luminosity fluctuations in the target. The expected rate in these forward detectors is about an order of magnitude higher than the rate of signal Møller electrons. Here, we plan to use quartz fibers alone, wrapped around the beam pipe in a manner that maximizes the efficiency of the transport of Čerenkov photons through the quartz fibers.

3.5 Electronics and Data Acquisition

This experiment employs a flux counting technique; the response of the calorimeter detectors is integrated over the duration of each beam pulse, and the helicity asymmetry is determined from this. The main component of the readout will be analog to digital converters (ADCs);

50-75 channels will be used to readout the scattered flux as well as beam position monitors and toroids to characterize each beam pulse. The ADCs used will have 16-bit precision; this is discussed in Sec. 3.5.1.

A block diagram of the DAQ system and electron beam control is shown in Fig. 13. Control of the electron beam parameters from the polarized source through most of ESA will be through the SLAC control program of the Main Control Center (MCC SCP) as is done at present (for E155). However, some corrector magnets in ESA will be perturbed periodically by the MCC SCP system under the direction of the Møller DAQ system. This is because small periodic perturbations must be made to the energy, position and angle of the electron beam in order to directly calibrate the effects of the beam parameters on the cross section, simultaneously with data taking. The principles underlying these procedures will be described in more detail in Sec. 4.1.2 and Appendix B.

The control of the electron beam polarization will be through the PMON system as is presently done; PMON will transmit the beam helicity, Pockels cell modes, Pockels cell voltages, half wave plate status, and an error bit to the ESA DAQ on each beam pulse as is currently done (for E155). For this experiment, there needs to be a link to get information quickly between the MCC SCP database and the Møller DAQ database. For example, monitoring of an ESA toroid by the Møller DAQ will be used to determine small correction voltages for the Polarized Source Pockels cells to null the helicity-correlated charge asymmetry in the electron beam, as described in App. A.

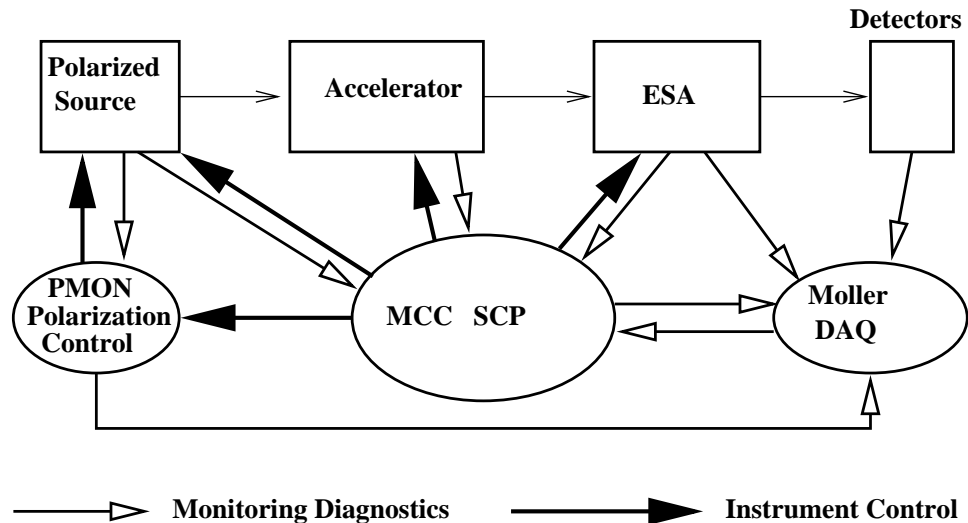


Figure 13: Diagram of DAQ System

3.5.1 Integrating ADCs

The integrated response of the calorimeter must be measured with a relative precision of 2×10^{-4} over the duration of each beam pulse. However, fluctuations in the beam parameters could degrade this uncertainty significantly. One must therefore measure the physical characteristics of the beam, such as energy, position and angle, with a relative precision better than 5×10^{-5} .

A cornerstone of this experimental technique is an ADC with true 16 bit precision. The ADCs are required to have integral nonlinearity at the level of 0.1% and differential nonlinearity at the level of 1 least significant bit. The sensitivity to the differential nonlinearity can be alleviated by adding a pseudo-random DC level to each integrated analog signal which is later subtracted off line. The ADC modules would be electrically shielded and the analog and digital grounds inside each module would be isolated to ensure optimum performance.

A working prototype of such an ADC has already been tested for a parity violation experiment at Jefferson Lab. It has demonstrated the required specification on differential nonlinearity and produced a resolution of 5×10^{-5} in beam tests. We plan to make a few minor improvements to this design and achieve 2×10^{-5} for this proposal.

3.6 Beam Polarimeter

The electron beam polarization measurement will employ a polarized target identical to that which was used for E154/E155[29]. A magnetized foil will be moved into the electron beam downstream of the hydrogen target. A pair of Helmholtz coils will produce a few 100 Gauss longitudinal magnetic field required for the alignment of the atomic electrons. Comparison of the raw asymmetry with the QED asymmetry for $\vec{e}^-\vec{e}^-$ scattering with appropriate dilution factors provides a determination of the beam polarization[30].

The same spectrometer setup that will be used to measure the electroweak asymmetry will also be used to carry out the beam polarization measurements. An additional outer collimator may be put in place during polarization measurements in order to limit the count rate in the detectors.

4 Systematic Uncertainties

4.1 Helicity Correlations

One of the challenging aspect of the experiment is to keep systematic errors at the level of a few parts per billion (ppb). The most important aspect is the rapid, pseudo-random flipping of the beam helicity on a pulse to pulse basis to minimize the effects of drifts. The experimental effort is then reduced to keeping the beam characteristics: position, angle, energy and phase space exactly the same for the two different beam helicities. For this experiment, we aim for an uncertainty of 3 ppb from possible helicity correlations.

We lay down the general principles to deal with systematic errors under helicity reversal.

- The differences of the beam parameters under helicity reversal must be minimized. The dominant correlations come from the laser light; its control is discussed in Sec. 4.1.1.
- The sensitivity of the cross section to beam parameters should be accurately measurable *simultaneously with data taking*, as discussed in Sec. 4.1.2 and Appendix B.
- The sign of the experimental asymmetry must be reversed by several different techniques or equivalently, many null asymmetries must be defined. This is discussed in Sec. 4.1.3.

4.1.1 Intensity Feedback

The sign of the beam helicity is changed pulse by pulse by controlling the handedness of the circularly polarized laser light incident on the photocathode of the polarized source. The laser circular polarization is in turn controlled by changing the polarity of the high voltage applied to a Pockels cell[¶] in the laser transport system. Most of the false asymmetries due to changes in the beam characteristics with helicity reversal can be traced back to helicity correlations of the laser intensity and position at the polarized source.

Obtaining negligible helicity correlations is not automatic; even a carefully prepared optical system can give rise to laser intensity asymmetries at the level of 100 parts per million (ppm). Indeed, during recent SLAC experiments, these asymmetries were maintained to be between 10 and 100 ppm using a feedback loop coupling the retardation of the Pockels cell

[¶]A Pockels cell is a crystal whose birefringence is proportional to the applied electric field across its face

and the intensity of the laser beam. A new feedback scheme will be implemented for this proposal, to gain two orders of magnitude further suppression. The basic method is described in Appendix A.

There is another, equally important reason for employing the laser feedback scheme. In the following section, we discuss the instrumentation required for monitoring beam parameters with high precision for the experiment. However, even if helicity correlations are reduced to a very small level, the actual corrections that are employed for a given experimental run would be dominated by the intrinsic beam parameter fluctuations, which are characteristics of the accelerator. One can see this quantitatively by comparing the values on the last column of Table 6 (the maximum allowable differences), with those on the previous column (anticipated differences from random fluctuations).

These corrections are reduced by the feedback scheme, which ensures that the cumulative average in the intensity asymmetry is smaller than that expected from statistical averaging. To the extent that the other beam parameters such as energy, position and angle are correlated with beam intensity, these corresponding cumulative averages will also be smaller than that expected from statistical averaging. The demonstration of small corrections is an important aspect of the experimental technique and will be a major goal of the low repetition rate pilot run (discussed in Sec. 5.1).

Beam Parameter	"Stat." Error per pulse		Jitter per pulse	Difference Over Entire Run	
	Measurement Error	$\delta(A_{LR})$		without feedback	goal with feedback
Intensity I	$3 \cdot 10^{-5} \cdot I$	$3 \cdot 10^{-5}$	$2 \cdot 10^{-2} \cdot I$	$8 \cdot 10^{-7} \cdot I$	$2 \cdot 10^{-7} \cdot I$
Energy E	$1 \cdot 10^{-5} \cdot E$	$1 \cdot 10^{-5}$	$4 \cdot 10^{-3} \cdot E$	$1.6 \cdot 10^{-7} \cdot E$	$2 \cdot 10^{-8} \cdot E$
Position	1 μm	$2.5 \cdot 10^{-5}$	100 μm	$4 \cdot 10^{-3} \mu\text{m}$	$4 \cdot 10^{-3} \mu\text{m}$
Angle	0.1 μrad	$4 \cdot 10^{-5}$	10 μrad	$4 \cdot 10^{-4} \mu\text{rad}$	$4 \cdot 10^{-4} \mu\text{rad}$

Table 6: Acceptable beam parameter uncertainties per pulse (Column II) and their impact on $\delta(A_{LR})$ per pulse (Column III). Column IV shows the intrinsic pulse to pulse fluctuations for various beam parameters. The last column lists the maximum acceptable cumulative helicity correlated asymmetries for $\delta(A_{LR})_{\text{sys}} \leq 1 \times 10^{-9}$ from each parameter.

4.1.2 Monitoring of Beam Parameters

The electron beam characteristics will be precisely measured for each beam pulse. To first order, the beam parameters depend on two position coordinates, two angle coordinates and energy. A set of 2 XY pairs of beam position monitors (BPMs) with a sufficient lever arm between them and a third BPM placed in the End Station where there is significant energy dispersion can span this space of 5 coordinates and thus characterize the electron trajectory for each beam pulse.

For example, the fractional energy resolution per pulse must be better than 5×10^{-5} , which is much smaller than the intrinsic energy fluctuations of 0.4%. The energy dispersion at the End Station bending magnet is known to be about 2cm/%[31]. The rated precision of the BPM in the A line bend is 50 μm averaged over the duration of a beam pulse. Thus, the energy can be measured with the required relative precision for each pulse. By proper placement of two sets of XY BPMs and toroids, the level of accuracy required to extract the noise contributions due to intensity, position and angle correlations can also be obtained. The toroid electronics will provide fractional intensity resolution per pulse of 3×10^{-5} and the BPMs at the target will provide a position resolution of 1 μm per pulse.

The impact of the monitoring precision on the statistical error per pulse of the measured cross section is listed in the third column of Table 6. The cumulative error on the asymmetry will be 7×10^{-5} per pulse, to be compared to the statistical fluctuations that range between $1.5 - 2.0 \times 10^{-4}$. This additional contribution to the statistical error is included in the projection of the final experimental error, tabulated in Table 8.

In order to determine the contributions from beam fluctuations to the measured asymmetry, a calibration method that monitors the sensitivity of the cross section to various beam parameters during data collections will be incorporated. Such a method has already been developed in previous experiments[4]. As described in Appendix B, steering coils and an energy vernier are slowly ramped during data taking and the response of BPMs to these changes are recorded. From this information, the correlations between fluctuations in the beam parameters and the cross section can be obtained.

4.1.3 Null Asymmetries

A powerful way to cancel systematic effects and prove the robustness of the measured asymmetry is to reverse the sign of the experimental asymmetry by a method which leaves the

sign of the systematic effects unchanged. We plan to change the sign of the asymmetry in two different ways: first by rotating a half-wave plate in the laser transport line and second by changing the beam energy. Additionally, we plan to measure A_{LR} in e-p scattering at $Q^2 \sim 0.003 \text{ (GeV/c)}^2$, which serves as a sensitive null experiment which will be carried out simultaneously.

Slow Helicity Reversal: At the ppb level, it is very easy to introduce false asymmetries in the experimentally measured asymmetry due to spurious electronic helicity correlations in the hardware. One way to reduce their impact is by changing the correspondence between the polarity of the voltage provided to the Pockels cell of the source laser and the sign of the electron beam. One way to accomplish this is by the introduction of a half-wave plate downstream of the Pockels cell. We expect that electronically induced false asymmetries are already suppressed at the level of 10 ppb. The sign change will provide approximately a further order of magnitude suppression.

g-2 Precession: Additional cancellation of spurious asymmetries from higher order helicity correlations in the electron beam such as phase space fluctuations will be obtained by running the experiment at two different beam energies. These energies correspond to pure longitudinal polarization of the electron beam in ESA. The higher energy corresponds to an additional 180° precession of the electron spin vector due to the $g - 2$ anomaly, thus effectively reversing the sign of the asymmetry. The figure of merit or analyzing power of the asymmetry measurement increases linearly with beam energy. On the other hand, one can achieve higher beam currents at lower beam energy. Based on these considerations, we plan to run 63% of the time at 48.3 GeV and the remaining time at 45 GeV, in order to achieve equal statistical uncertainties on the two oppositely signed raw asymmetries.

Ideally, the reversals should be carried out when the statistical error begins to approach the size of the largest potential systematic error. The statistical error in each day of data would be 0.1 ppm. The half-wave plate flips would be carried out once a day and the beam energy on target would be changed once every several days.

Very Forward Angle e-p Scattering: An important cross check will be obtained by monitoring the asymmetry in very forward angle e-p scattering using an auxiliary detector very close to the beam line. The scattering angle in the laboratory frame is about 1 mrad. The estimated rate is 10 times the rate of Møller electrons and the electroweak asymmetry is expected to be 20 times smaller than the Møller asymmetry. The estimated asymmetry will

thus be roughly 10 ppb and the statistical error should be about 3 ppb. The measurement of the e-p asymmetry therefore becomes a sensitive null experiment which can be carried out simultaneously with the actual measurement.

4.2 Longitudinal Beam Polarization

As mentioned in the introduction, the error on $\sin^2 \theta_W$ extracted from the Møller asymmetry, which quantifies the sensitivity of the measurement as a test of the electroweak theory, is less sensitive to normalization errors since the asymmetry is proportional to $1 - 4 \sin^2 \theta_W$. This implies that the conventional single arm Møller polarimeter should be sufficient for the experiment. Nevertheless, we expect that this will be the largest contribution to the systematic error in the experiment.

If the asymmetry is measured once every few shifts, it should be easy to achieve a fractional statistical error on the beam polarization of 1%. There are several sources of systematic error. The background from radiative Mott scattering is typically 10% and the systematic error from the background subtraction would be $\sim 1\%$. Target and spectrometer geometry would contribute a fractional systematic error at the level of 1%. The dominant error comes from the measurement of the foil polarization which is typically around 2% [32]. Target non-uniformities will be eliminated by using several foils. We will assume a total systematic error of 2.7%, which has been achieved in several previous experiments [29]. This would contribute an error on $\sin^2 \theta_W$ of ± 0.00030 .

4.3 Physics Backgrounds

The spectrometer and detector geometry have been carefully chosen so that the only relevant backgrounds are those that are produced in the same range of laboratory scattering angles that corresponds to the range of scattered Møller electrons of interest. These background processes can be grouped in three categories: inelastic electron-proton scattering of beam energy electrons, elastic and inelastic scattering of the electron radiative tail and real and virtual photoproduction of pions.

The estimates of the contribution of the backgrounds to the total rate at the detector as well as the relative contributions to the measured asymmetry are discussed in detail in Appendix C. The results are summarized in Table 7. These estimates are expected to be

guidelines. Additional work with the world electroproduction and photoproduction data and cross checks with special background runs should make the estimates more precise. The general indications are that one or two of the backgrounds could make contributions to the asymmetry which are significant fractions of the statistical error.

Process	σ/σ_M	δA
Inelastic $e - p$	0.002	0.02
elastic $e - p$	0.15	0.07
Δ Electroproduction	2.5×10^{-3}	0.01
Resonance Electroproduction	3.0×10^{-3}	0.01
Other Electroproduction	2.0×10^{-3}	0.01
π s from DIS	1.3×10^{-5}	0.01
π s from $\gamma - p$	0.013	0.015
π s from $\gamma^* - P$	0.002	0.013

Table 7: Summary Table of Physics Background Estimates

We will dedicate some beam time to study some of these backgrounds. We note that the most important backgrounds from pion production and elastic scattering off the proton of the electron radiative tail will be directly estimated during the experiment with supplementary detectors. We plan to monitor the elastic e-p electroweak asymmetry with a separate calorimeter, since these electrons are separated from Møller electrons by the spectrometer (See Sec. 3.3.4).

4.4 Radiative Corrections

The contributions from the quark loops in Fig. 3a cannot be accounted for perturbatively. Instead, one uses a dispersion relation to relate those vacuum polarization effects to $e^+e^- \rightarrow$ hadrons data. The authors of Ref. [7] assign a conservative error to this contribution, corresponding to $\delta(\sin^2 \theta_W) \sim 0.00055$. It is expected that a careful treatment of the isospin decomposition of the effects should reduce this error by a factor of four[33], sufficient to make the contribution to the overall projected error in the measurement small.

The remaining corrections come from many additional diagrams such as WW and ZZ box diagrams, vertex corrections, two boson exchange diagrams and additional small corrections to account for the fact that the Q^2 of the experiment is not exactly zero. The

Beam Energy (GeV)	48.3	45.0
incident e^- s per pulse	3.5×10^{11}	6×10^{11}
detected e^- s per pulse	2.5×10^7	4.5×10^7
$\delta(A_{LR})$ per pulse	2.02×10^{-4}	1.49×10^{-4}
$\oplus 7 \times 10^{-5}$	2.14×10^{-4}	1.65×10^{-4}
% running time	63	37
# of pulses (at $\epsilon = 0.43$)	3.93×10^8	2.31×10^8
$\delta(A_{LR})$	1.08×10^{-8}	1.08×10^{-8}
$\delta(\sin^2 \theta_W)$	0.00099	0.00106

Table 8: Estimated statistical error for a 20 week production run at 43% efficiency

theoretical uncertainties in these corrections are negligible. The effect of bremsstrahlung on the theoretical prediction will depend on the detector geometry and the spectrometer design. On general grounds, the authors of Ref. [7] argue that the effects will be small and calculable with high accuracy. The reason is that soft photon effects, including radiation damping, factorize and cancel in the asymmetry ratio. The same should be true to a large extent for hard bremsstrahlung, though it needs to be checked for the final experimental setup.

The net effect of the radiative corrections is to reduce the tree level prediction by 40%, where the main uncertainty comes from the vacuum polarization loops. This reduction of the tree level prediction can be attributed to an increase $\sin^2 \theta_W$ by 3% in running from $Q^2 = M_Z^2$ to 0. The reduction has no effect on the projected statistical sensitivity of the experimental measurement. In fact, it alleviates systematic errors such as the beam polarization, which enter as an overall normalization on the measured experimental asymmetry.

4.5 Summary of Uncertainties

As discussed earlier, we plan to measure the asymmetry with equal precision at two different beam energies. We summarize the important parameters for accumulation of the data in a 20 week production run in Table 8. The estimates of the scattered flux are based on the simulations discussed in Sec. 3.3.4.

We summarize the goals for the upper limits on various systematics errors on the raw asymmetry in Table 9. To extract a measurement of the weak mixing angle, it is necessary to

first apply several scale factors to obtain the effective electroweak coupling. We list the dominant contributions to the uncertainty on $\sin^2 \theta_W$ from various normalization uncertainties in Table 10.

Statistical Error	7.1
Beam Properties	< 3
Electronics Crosstalk	< 1
Transverse Polarization	< 1
Magnetized Iron Background	< 1
Beam Phase Space	< 1

Table 9: Error Contributions to the Raw Asymmetry in Parts per Billion

Beam Polarization	≤ 0.0003
Radiative Corrections	< 0.0001
Background Subtraction	< 0.0001
Estimation of $\langle Q^2 \rangle$	< 0.0001

Table 10: Normalization Error Contributions to the Measurement of $\sin^2 \hat{\theta}_W(0)$

5 Proposed Run Plan

5.1 Tests and Milestones

To make efficient use of accelerator time, we plan to satisfy the following milestones before taking production data:

1. Establish stable running of the laser light at the photocathode, limiting the average helicity correlated intensity asymmetry to be less than 10^{-7} .
2. Establish the same stability with the electron beam. The first tests could be carried out parasitically, during an SLD run, with no negative impact on machine efficiency.
3. Establish that the accelerator is capable of providing a stable electron beam satisfying the criteria listed in Table 4.
4. Establish stable running conditions with the target, spectrometer and detectors installed in a two week test run at low repetition rate.

Item 1 should demonstrate that it is possible to control the cumulative average helicity correlated intensity asymmetry in the laser light at a level between 10 and 100 ppb. No electron beam is required for this test. Item 2 is a quick test to demonstrate that the same

stability is achievable with the electron beam. Item 3 and 4 will require a dedicated test at low repetition rate lasting at least one week.

Item 4 allows the first look at the full experimental setup and would allow an initial shakedown of the entire apparatus. The goals would be to establish that the detectors work at the required efficiency and that the backgrounds are under control at the estimated level. Additionally, the ability of the beam line monitoring instrumentation to keep systematic errors under control will be demonstrated. The above milestones will be quantified in detail so that their success would imply that the goals for the statistical and systematic errors described in previous sections are achievable during the production run.

5.2 Production Running

Items 3 and 4 could be carried out well before the main experimental run. To achieve the stated statistical error, the experiment requires a total integrated charge of 2.25×10^{20} electrons, which can be realistically achieved in 20 calendar weeks. Once stable running is established, the efficiency of obtaining data in the End Station parasitic with PEP-II is expected to be 43%. The estimates of the statistics from a 20 week production run is listed in Table 8.

5.3 Beam Time Request

Running Mode	Repetition Rate	Calendar Weeks	Purpose
Test	30 Hz	2	Hardware Checkout
Production	30 Hz	1	Beam Checkout
Production	120 Hz	20	Production Data
Production	30 Hz	1	Backgrounds

Table 11: Summary of Beam Time Request

For running in End Station A, we request a 2 week run at 30 Hz to carry out a complete checkout of the apparatus and demonstrate the desired systematic control. Such a test could possibly be carried out significantly before production running. For production data, we request 22 weeks of beam time, of which 20 weeks will be at 120 Hz. We propose to use the first week at low repetition rate for general shakedown of the experimental equipment,

which should be sufficient, given the experience of the earlier run. We then propose to use the next 20 weeks to accumulate production data. A total of one week at low repetition rate will be required for background studies. The beam time request is summarized in Table 11.

6 Summary

We propose to measure the electroweak asymmetry in Møller scattering using the 50 GeV polarized electron beam at SLAC. In a 20 week production run, the weak mixing angle $\sin^2 \hat{\theta}_W(0)$ would be measured with a total error of 0.0008. This would explore electron compositeness scales exceeding 10 TeV. The potential to measure a purely leptonic weak neutral current coupling at $Q^2 \ll M_Z^2$ is unprecedented. The experimental measurement would set a new standard for precision electroweak experiments at low Q^2 . *The combined requirements of low systematic errors, high intensity and high polarization at the electron source as well as high incident energy on target makes SLAC the only existing laboratory at which this measurement can be carried out.*

Acknowledgements

We would like to thank Bill Marciano and Michael Peskin for important discussions and comments.

A Intensity Feedback at the Polarized Source

A.1 Existing Polarized Electron Source (PES)

A schematic of the current SLAC Polarized Electron Source[34] is shown in Fig. 14. Polarized electrons are produced by photoemission from a GaAs photocathode. Different laser light sources are used for ESA and SLC physics programs due to the different pulse structures required (see Table 12). For ESA, a flashlamp-pumped Ti:sapphire laser is used to produce one 100-350ns pulse.

The laser is polarized with a linear polarizer and two Pockels cells. The axes of the linear polarizer and the PS Pockels cell are along the x,y axes, while the axes of the CP Pockels cell are along u,v (u,v axes are rotated by 45° with respect to x,y). This configuration can

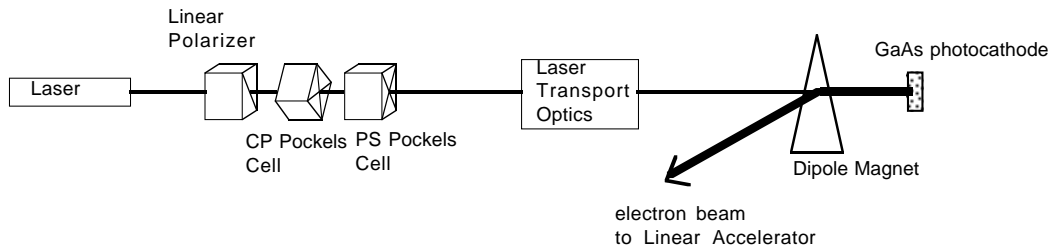


Figure 14: SLAC Polarized Electron Source

generate arbitrary elliptical polarization, and can compensate for phase shifts in the laser transport optics. The laser circular polarization, \mathcal{P}_γ , at the GaAs photocathode is well approximated by $\mathcal{P}_\gamma = \sin\left(\frac{V_{CP} - V_{CP}^T}{V_{\lambda/4}} \cdot \frac{\pi}{2}\right) \cos\left(\frac{V_{PS} - V_{PS}^T}{V_{\lambda/4}} \cdot \frac{\pi}{2}\right)$, where V_{CP} and V_{PS} are the Pockels cell voltages; $V_{\lambda/4}$ is the Pockels cell quarter-wave voltage; V_{CP}^T and V_{PS}^T are phase shifts induced by the laser transport optics.

To generate circular polarized light, one nominally operates the CP Pockels cell at its quarter-wave voltage and the PS cell at 0 Volts. Small corrections to these voltages are needed to compensate for phase shifts in the transport optics to the photocathode. A positive HV pulse on the CP Pockels cell produces one helicity, while a negative HV pulse produces the opposite helicity. The sign of this HV pulse is set by a pseudo-random number generator, which updates at 120 Hz (the electron beam pulse rate).^{||}

Two problems encountered with the GaAs photoelectron source are the *Charge Limit*[36] and the *Charge Asymmetry*[37]. Charge Limit is a phenomenon whereby the instantaneous photocathode QE decreases appreciably due to high incident light fluxes, and thereby limits the maximum electron charge that can be extracted. Experimentally one finds that the maximum extracted charge is proportional to the QE at low incident light fluxes and is independent of the maximum laser power available. In practice, this has not severely impacted the performance of the polarized electron source at SLAC, but it is an issue that

^{||}The algorithm for the pseudo-random number generator is described in P. Horowitz and W. Hill, *The Art of Electronics*, pp. 437-442, Cambridge University Press, Cambridge (1980). Knowledge of the polarization bits on thirty-three consecutive machine pulses is sufficient to determine the future polarization bit sequence. The use of this algorithm allows the experimenters to monitor the integrity of the polbit transmission system. The polbits are transmitted by 2 independent schemes to the experiment from the polarized source to the experiment, and this transmission includes information on the Pockels cell mode (random, alternating left/right, fixed left or fixed right), error checking of the voltage applied to the Pockels cell and a checksum bit.

Parameter	E154	E155	SLD
N^- (at experiment)	$1 \cdot 10^{11}$	$4 \cdot 10^9$	$3.8 \cdot 10^{10}$
f_{rep}	120 Hz	120 Hz	120 Hz
Pulse Length (at source)	200ns	200ns	2ns
Beam Energy (at experiment)	48.6 GeV	48.6 GeV	46.6 GeV
Polarization (at experiment)	82%	85%	77%
Run time	2 months	3 months	4 months
Year	1995	1997	1996

Table 12: Beam Parameters for recent SLAC experiments

needs to be addressed for photocathode electron sources.

The Charge Asymmetry problem results from small linear polarized components in the laser beam and a dependence of the electron yield on the orientation of the linear polarization. For laser light which is 100% linear polarized, 10% variations in the electron yield have been observed depending on the orientation of the linear light polarization. This effect results from anisotropies in the strain[37]. Even light with $\mathcal{P}_\gamma = 99.5\%$ has 10% linear polarization, and appreciable charge asymmetries between the *right* and *left* beam polarization states at the 1% level can result. In practice, this is an easy problem to fix by monitoring the electron beam charge asymmetry and controlling the Pockels cell voltages to null the asymmetry. For the SLAC source, the PS Pockels cell voltage is controlled to null the charge asymmetry in a feedback loop. It is easy to maintain the asymmetry below 10^{-4} and the level of the average asymmetry is only limited by the sophistication of the feedback algorithm and the statistical fluctuations in the electron charge.

A.2 PES Modifications

The requirements of the polarized beam for the proposal are tabulated in Table 4. To achieve the required beam current, $(4 - 7) \times 10^{11}$ electrons per pulse are required at the injector. The polarized source specification that needs significant improvement for the Møller proposal is the size of the electron *charge asymmetry* between the two polarization states (*left* and

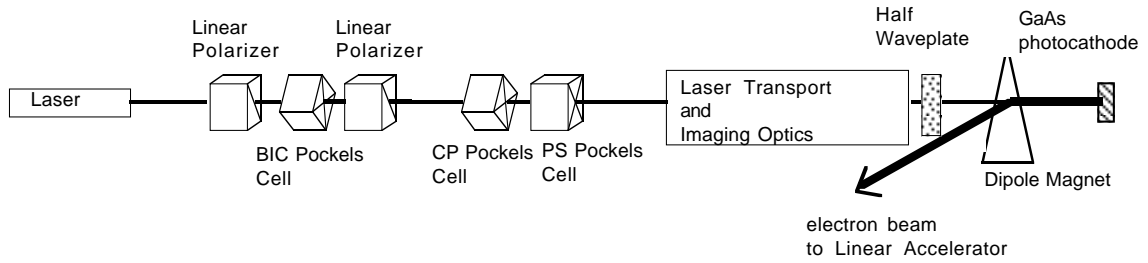


Figure 15: Polarized Electron Source for this Experiment

right) of the beam. The main source of this asymmetry arises from small linear polarization components of the laser light and strain anisotropy in the photocathode, as was described in the previous section. Small contributions to the asymmetry also arise from transmission asymmetries in the laser transport optics (again due to residual linear polarization of the laser light[38]), and from steering effects of the CP Pockels cell. These steering effects can be minimized by imaging the CP Pockels cell onto the photocathode.

The proposal aims to measure an experimental *left-right* asymmetry with a statistical precision of 7×10^{-9} and a systematic error of 3×10^{-9} in 5 months of running at 43% efficiency. The run will have 6×10^8 pulses, which will require that the beam charge per pulse be measured with an accuracy better than $3 \cdot 10^{-5}$.

In addition to measuring the charge asymmetry very accurately with toroids at the level of 10^{-9} (averaged for the whole run), it is desirable to keep the charge asymmetry to be corrected as small as possible and preferably below 10^{-7} . We note that the intensity fluctuations per pulse of the beam are expected to be about 2%, so that for the 5 month run one would expect a charge asymmetry just from statistical fluctuations to be a few parts in 10^7 . This can, however, be significantly reduced by a charge asymmetry feedback algorithm which corrects for cumulative charge asymmetries as described below.

The proposed polarized source configuration is shown in Fig. 15. An additional half-wave plate is included for reversing the beam helicity independently from the CP Pockels cell. This can be done on a slow time scale (for example, every several hours) and can be used to check and cancel false asymmetries generated by the CP Pockels cell. To correct for charge asymmetries, a Bunch Intensity Control (BIC) Pockels cell system is included. Based on experience in previous experiments, these modifications should suffice to achieve the level of systematic control required to carry out the experiment.

A.3 Intensity Feedback Algorithm

Rather than feeding back on the PS Pockels cell voltage to null any charge asymmetries as is done for the current SLAC source, we propose to use the BIC Pockels cell system which has a known transfer function and is more stable. We assume that the BIC system introduces a charge asymmetry, A^{BIC} , and that the system from the CP Pockels cell to the photocathode introduces a charge asymmetry, A^C . The beam charge asymmetry for a run N is then given by

$$A_N^{beam} = A_N^{BIC} + A^C + A_N^{stat}$$

where A_N^{stat} is due to statistical fluctuations.

The proposed feedback algorithm to reduce the charge asymmetry is:

$$A_1^{BIC} = 0$$

$$A_N^{BIC} = A_{N-1}^{BIC} - A_{N-1}^{beam}$$

The results of this feedback algorithm on the beam charge asymmetry is shown in Table A.3.

The average beam charge asymmetry will be given by

$$\begin{aligned} \langle A^{beam} \rangle &= \frac{1}{N} \sum_{i=1}^N A_i^{beam} \\ \langle A^{beam} \rangle &= \frac{A^C}{N} + \frac{A_N^{stat}}{N} \end{aligned}$$

This algorithm employs correcting the cumulative charge asymmetry to achieve a $1/N$ scaling reduction. For example, if the feedback runs have 2,000 pulses then there will be $2.5 \cdot 10^5$ runs in the experiment and each run will have a typical statistical charge asymmetry of $5 \cdot 10^{-4}$. It is easy to achieve $A^C < 10^{-3}$ by appropriate settings of the CP and PS Pockels cell voltages. Thus, the beam asymmetry averaged over the entire run will be less than 10^{-8} , and this can be corrected for by accurate toroid measurements to better than $2 \cdot 10^{-9}$.

B Calibration of Sensitivity to Beam Parameters

During data taking, the beam parameters would be varied (at rates that are slow compared to the helicity flipping frequency) in a controlled way by perturbing corrector coils to vary position and angle as well as a radiofrequency module to vary the energy. To correct the

Run Number	A_N^{BIC}	A_N^{beam}
1	0	$A^C + A_1^{stat}$
2	$-A_C - A_1^{stat}$	$-A_1^{stat} + A_2^{stat}$
3	$-A^C - A_2^{stat}$	$-A_2^{stat} + A_3^{stat}$
N	$-A^C - A_{N-1}^{stat}$	$-A_{N-1}^{stat} + A_N^{stat}$

Table 13: Beam Charge Asymmetry Beam Parameters

raw asymmetry, we use the equation

$$A_{\text{exp}} = A_{\sigma} - a_i \delta M_i, \quad (14)$$

where A_{σ} is the uncorrected asymmetry, δM_i are the helicity correlated differences in the BPMs and a_i are correction coefficients.

The correction coefficients a_i , which are equivalent to $\partial\sigma/\partial M_i$, are computed by first measuring the response of the cross-section and BPMs to coils C_j : $\partial\sigma/\partial C_j$ and $\partial M_i/\partial C_j$. The a_i are then obtained by solving the matrix equation:

$$\frac{\partial\sigma}{\partial C_j} = \frac{\partial\sigma}{\partial M_i} \frac{\partial M_i}{\partial C_j} = a_i \frac{\partial M_i}{\partial C_j}. \quad (15)$$

The key to the success of the method is to ramp, under computer control, a complete set of parameters with devices placed upstream of all BPMs. There are important dynamic range criteria to be considered. Firstly, the coils must vary the position and angle with ample independence so that the matrix $\partial M_i/\partial C_j$ is far from being singular, since it must be inverted to obtain the coefficients. The amplitude of the ramping must be large enough to exceed the normal beam jitter but small enough so that the statistical error on the cross-section is not degraded. This method is crucial to be able to take production data and study systematic errors simultaneously.

C Estimates of Physics Backgrounds

There are a number of backgrounds to Møller scattering listed below which are grouped into three categories; inelastic electron-proton scattering, scattering of the electron radiative tail,

and pions. The abbreviation in square brackets will serve to identify the various processes in the rest of the document.

1. Inelastic scattering of full energy electrons from protons. [*Inel*]
2. Scattering of electron radiative tail from protons.
 - (a) Elastic scattering. ($M = 0.938 \text{ GeV}/c^2$). [*el*]
 - (b) Delta resonance ($W = 1.23 \text{ GeV}/c^2$). [Δ]
 - (c) Other resonances. ($W = 1.3\text{-}1.7 \text{ GeV}/c^2$). [*Res*]
 - (d) Other inelastic scattering ($W > 1.7 \text{ GeV}/c^2$). [$W > 1.7$]
3. Pion production.
 - (a) Deep inelastic scattering [*DIS*].
 - (b) π from γP scattering with real photons. Parity violating $\rho - N$ coupling may contribute to the asymmetry. [γP]
 - (c) Pions from virtual photon scattering. Both $\rho - N$ and $e\rho$ couplings may violate parity. [$\gamma^* P$]

The corrections to the Møller asymmetry due to these backgrounds is computed as follows. Assume that the backgrounds have N_B counts with an asymmetry A_B contaminate N_M Møller counts with asymmetry A_M . Then

$$A_{obs} = A_M - \frac{N_B(A_M - A_B)}{N_M + N_B}$$

We can approximate this into two factors, a dilution factor due to high rates with little asymmetry

$$f = N_B/N_M$$

and

$$\delta A = \frac{N_B A_B}{N_M A_M}$$

Ideally, both are small compared to our projected error in $\delta A_M/A_M$ of 0.03. The relevant numbers are $\sigma_M = 14 \text{ } \mu\text{barn}$ and $A_M = 3 \times 10^{-7}$.

C.1 General Formalism

The cross section can be computed making reasonable approximations as follows. First, we list the general formulae for kinematic variables and cross sections:

E = incident electron energy

E' = scattered electron energy

$\nu = E - E'$ $y = \nu/E$

$$Q^2 = 4EE' \sin^2 \frac{\theta}{2} = 2MExy \rightarrow EE'\theta^2 : x = \frac{Q^2}{2M\nu} : \tau = \frac{Q^2}{4M^2}$$

$$\frac{d^2\sigma}{dE'd\Omega} = \frac{\alpha}{2\pi^2 Q^2} \frac{E'}{E} \frac{|\mathbf{K}|}{1-\varepsilon} [\sigma_T + \varepsilon_L \sigma_L]$$

$$|\mathbf{K}|^2 = |\mathbf{k}|^2 = Q^2 + \nu^2$$

$\varepsilon = \left(1 + 2\frac{|\mathbf{k}|^2}{Q^2} \tan^2 \theta/2\right)^{-1}$ is the virtual photon polarization.

$$\varepsilon_L = \frac{Q^2}{\nu^2} \varepsilon$$

$W^2 = M^2 + 2M\nu - Q^2$ is the missing mass squared.

$$\frac{d^2\sigma}{dx dy} = \frac{\pi\alpha^2 F_2}{MEx^2y^2} (2 - 2y + y^2) \text{ for DIS if } F_2 = 2xF_1$$

For most of the relevant kinematics for inelastic scattering ε_L is small and is usually neglected. The opposite is true for elastic scattering where $\varepsilon_L = \varepsilon/\tau$.

For our case with electron scattering, where $p_\perp = \sqrt{Em/2} = 0.113 \text{ GeV}/c$, the Q^2 is small $\approx 0.025 \text{ (GeV}/c)^2$ and $Q^2 \ll \nu$. The dominant process is the scattering of barely virtual photons.

C.2 Inelastic Scattering from the Proton

The first background to Møller scattering is inelastic scattering of beam electrons with the full beam energy from the protons in the target. Here the appropriate limits are $\theta \ll 1$ and $Q^2 \ll \nu^2$. Thus we have to good approximation

$$\frac{|\mathbf{K}|}{1-\varepsilon} = \frac{E^2 + E'^2}{\nu}$$

$$\frac{d^2\sigma_{Inel}}{dE'd\Omega} = \frac{\alpha}{2\pi^2 Q^2} \frac{E'}{E} \frac{E^2 + E'^2}{\nu} \sigma_T = \frac{\alpha}{2\pi^2 \nu \theta^2} \left[1 + \left(\frac{E'}{E}\right)^2\right] \sigma_T$$

Finally

$$\begin{aligned}\sigma_{Inel} &= \frac{\alpha}{\pi} \int_{.12}^{.25} \left[1 + \left(\frac{E'}{E}\right)^2\right] \sigma_T \frac{dE'}{\nu} \int \frac{d\theta}{\theta} = \frac{\alpha}{\pi} \int_{.50}^{.76} \frac{dy}{y} [2 - 2y + y^2] \sigma_T \int \frac{d\theta}{\theta} \\ &\approx \frac{0.41\alpha}{\pi} \ln \frac{\theta_{max}}{\theta_{min}} \sigma_T \approx 0.04 \mu\text{barns}\end{aligned}$$

where we have used $\sigma_T \approx 100 \mu\text{barns}$ and assumed to be approximately constant. θ_{max} and θ_{min} are the range over theta where an electron of energy E' is accepted by the detector.

The result is $\approx 0.04 \mu\text{barns}$ or 0.2% of the Møller cross section. The asymmetry is probably 10 times higher because the σ_T is dominated by the ρ resonance which likely has an isovector coupling to the Z .

C.3 Electroproduction of the Delta from Radiated Electrons

Radiative elastic scattering (Process 2a) from protons was computed using a GEANT simulation and contributes 13% to the Møller signal. This is dominated by electrons that radiate externally before the elastic scattering. The same is true for electroproduction (processes 2b, 2c, and 2d). Thus it is sufficient to calculate the ratio of the various processes to that of elastic scattering.

For Process 2b, $\nu = 0.340 + 2\tau \approx 0.340 \text{ GeV}$. Useful relations for *elastic* scattering are:

$$\varepsilon_{el} = \left(1 + 2(1 + \tau) \tan^2 \frac{\theta}{2}\right)^{-1}$$

$$E'_{el} = E / \left(1 + 2(E/M) \sin^2 \frac{\theta}{2}\right)$$

$$\lim_{\theta \rightarrow 0} \frac{d\sigma_{el}}{d\Omega} = \frac{\alpha^2 E'}{4E^3 \sin^4 \frac{\theta}{2}}$$

For inelastic scattering with $\cos^2 \frac{\theta}{2} \rightarrow 0$

$$\frac{|\mathbf{K}|}{1 - \varepsilon} \rightarrow 2EE' / |\mathbf{K}|$$

$$\lim_{\theta \rightarrow 0} \frac{d\sigma}{d\Omega dE'} = \frac{\alpha E' \sigma_T}{4\pi^2 E |\mathbf{K}| \sin^2 \frac{\theta}{2}}$$

$$R_{\Delta} \equiv \frac{\sigma_{\Delta}}{\sigma_{el}} \rightarrow \frac{E^2 \sigma_T \Delta E \sin^2 \frac{\theta}{2}}{\pi^2 \alpha |\mathbf{K}|} \rightarrow \frac{Q^2 \Delta E}{4\pi^2 \alpha |\mathbf{K}|} \sigma_T$$

$$R_{\Delta} \approx \frac{(0.01)(0.120)}{4\pi^2 \alpha (.340)} 1.5 = 0.017$$

where we used $\sigma_T = 600\mu\text{barns} = 1.5/(\text{GeV})^2$ and $\Delta E = 0.120$.

$$f_\Delta = \frac{N_\Delta}{N_M} = \frac{N_\Delta}{N_{eP\text{ el}}} \frac{N_{eP\text{ el}}}{N_M} = (0.15)(0.017) = 2.5 \times 10^{-3}$$

The asymmetry is about five times larger than the Møller asymmetry, since the coupling is about ten times larger and the average Q^2 is smaller by a factor of two. Therefore, $\delta A_\Delta \approx 0.01$

C.4 Electroproduction of Other Resonances from Radiated Electrons

For additional resonances, we use the relation

$$\frac{\Delta E}{\nu} \sigma_T \approx \frac{(.600)(.120)}{.34} \approx 0.21 \rightarrow \sigma_T \int \frac{dE'}{\nu} = -\sigma_T \int \frac{d\nu}{\nu} = \sigma_T \ln \frac{\nu_{max}}{\nu_{min}}$$

For $W=1.3$ GeV, $\nu = 0.43$ GeV, while for $W=1.7$ GeV, $\nu = 1.1$ GeV, and since there are few elastic scatters for $E > 20$ GeV, the largest ν is ≈ 10 GeV. The cross section is $300\mu\text{barns}$ for most of the resonances and $100\mu\text{barns}$ for the continuum. Thus the resonance region and the higher massed each contribute 50% more than the Δ resonance. In total we estimate

$$f_{res} = 0.01, \quad \delta A_\Delta \approx 0.03$$

C.5 Deep Inelastic Scattering

Electrons from deep inelastic scattering (DIS) are produced at large angles with respect to the spectrometer acceptance but pions from DIS are a small background. The problem is that $A_{DIS} \approx 10^{-4}Q^2$, a factor of 1000 times greater than from Møller scattering, where Q^2 is 0.03 $(\text{GeV}/c)^2$.

$$\frac{d^2\sigma_{DIES}}{dxdy} = \frac{\pi\alpha^2 F_2}{ME^2 x^2 y^2} (2 - 2y + y^2)$$

where $F_2 \leq 0.4$. This must be integrated with the limits $x < 1$, $y < 1$, and $2MExy > Q_{min}^2$. Normally for DIS one uses $Q_{min}^2 = 1$ GeV^2 . A lower value of 0.2 is probably more accurate. However, the differences are unimportant for the present level of accuracy.

$$\begin{aligned} \int \frac{d^2\sigma_{DIS}}{dxdy} dxdy &= \frac{2\pi\alpha^2}{Q_{min}^2} \int \frac{(2 - 2y + y^2)}{y} dy \\ &= \frac{2\pi\alpha^2 F_2}{Q_{min}^2} \left(-2 \ln y_{min} - \frac{3}{2} + 2y_{min} - \frac{1}{2} y_{min}^2 \right) \\ &= 0.10\mu\text{barns} \end{aligned}$$

We have used $Q_{min}^{-2} = 400\mu\text{barns}$ for $Q_{min}^2 = 1(\text{GeV}/c)^2$. To estimate y_{min} , we note that a background pion must have at least 10 GeV, so $\nu > 10$ GeV or $y_{min} = 0.2$. We use this value in our estimate. The kinematic limit for y_{min} is $(2ME)^{-1} \approx 0.01$, $(\text{GeV})^{-2}$ which only doubles the cross section. The result is that the cross section is negligible, so pions from DIS do not contribute significantly to the background rate.

Next we compute the average Q^2 for the total DIS cross section, which is proportional to the asymmetry. We have

$$\langle Q^2 \rangle = \int_{x_m}^1 \int_{y_m}^1 Q^2 \sigma(x, y) dx dy / \int_{x_m}^1 \int_{y_m}^1 \sigma(x, y) dx dy$$

where

$$\sigma \propto \frac{2 - 2y + y^2}{x^2 y^2}, \quad Q^2 = 2MExy \quad \text{and} \quad x_{min} = \frac{Q_{min}^2}{2MEy}$$

Then

$$\begin{aligned} \int_{x_m}^1 \int_{y_m}^1 \frac{2 - 2y + y^2}{x^2 y^2} dx dy &= \frac{2ME}{Q_{min}^2} \int_{y_m}^1 \frac{2 - 2y + y^2}{x^2 y^2} dy \\ &= \frac{2ME}{Q_{min}^2} \left[2 \ln y - 2y + \frac{1}{2} y^2 \right]_{y_m}^1 \\ &= \frac{2ME}{Q_{min}^2} \left(-2 \ln y_{min} - \frac{3}{2} + 2y_{min} - \frac{1}{2} y_{min}^2 \right) \end{aligned}$$

For the numerator, we remember

$$\begin{aligned} \int \ln(ax) dx &= x \ln(ax) - x : \quad \int x \ln(ax) dx = \frac{x^2}{2} \ln(ax) - \frac{x^2}{4} : \\ \int x^{-1} \ln(ax) dx &= \frac{1}{2} \ln^2(ax) \end{aligned}$$

Then the numerator is

$$2ME \int_{x_m}^1 \int_{y_m}^1 \frac{2 - 2y + y^2}{xy} dx dy = 2ME \int_{y_m}^1 \ln\left(\frac{2MEy}{Q_{min}^2}\right) \frac{2 - 2y + y^2}{y} dy \quad (16)$$

$$= 2ME \left[(\ln^2(ay) - 2y \ln(ay) + 2y + \frac{y^2}{2} \ln(ay) - \frac{y^2}{4}) \right]_{y_m}^1 \quad (17)$$

where $a \equiv 2ME/Q_{min}^2$. The result is $\approx 2Q_{min}^2$. This gives $(A\sigma)_{DIS}/(A\sigma)_{M=5}$. This ratio varies slowly with Q_{min}^2 , indeed approximately as $\ln^2(Q_{min}^2/2ME)$. If we estimate one pion per event with $p=10$ GeV with a typical $p_{\perp} = 1$ GeV, 1% will enter our acceptance. If 20% of the energy is deposited in the lead glass, the contamination is a negligible 1% of A_{LR} . Measuring this contribution is possible only with a coincidence experiment, since photoproduction produces most of the pions with these kinematics. We do not currently plan to study this effect.

C.6 Pion Production by Real and Virtual Photons

The cross section for real photons to interact is $\sim 100\mu\text{barns}$. Assuming 0.2 photons/electron and a 1/500 suppression for pions (mostly coming from acceptance) as assumed for DIS, the contribution to the signal is about 0.5%. The parity violating asymmetry should be of the same order as that measured in elastic pp scattering. In that case, the asymmetry will be of the same order as A_{LR} .

To estimate virtual pion production, we must integrate the result from a previous section

$$\sigma_{\gamma^*P} = \frac{\alpha\sigma_T}{\pi} \int \int \frac{d\theta}{\theta} \frac{dy}{y} [2 - 2y + y^2] = \frac{\alpha\sigma_T}{\pi} \int \ln\left(\frac{\theta_{max}}{\theta_{min}}\right) \frac{dy}{y} [2 - 2y + y^2]$$

over all allowed y .

This total photoproduction cross section diverges in the usual approximation that the electron mass is zero. Expanding in powers of m_e^2 , we have

$$Q^2 = 4EE' \sin^2 \frac{\theta}{2} + \frac{m_e^2 \nu^2}{EE'}$$

which does not vanish at $\theta = 0$ for *inelastic scattering*. For the integrals, we use the cutoff

$$Q_{min}^2 \approx EE'\theta^2 \approx \frac{m_e^2 \nu^2}{EE'} \Rightarrow \theta_{min} = \frac{m_e \nu}{EE'} = \frac{m_e y}{E(1-y)}$$

The requirement $Q^2 \approx EE'\theta^2 < 1 \text{ GeV}^2$ yields

$$\theta_{max} = \frac{Q_{max}}{E\sqrt{1-y}}$$

Thus

$$\ln\left(\frac{\theta_{max}}{\theta_{min}}\right) = \ln\left(\frac{Q_{max}}{m_e} \frac{\sqrt{1-y}}{y}\right) \approx \ln\left(\frac{Q_{max}}{m_e}\right)$$

Since $Q_{max} \gg m_e$, the y -dependence inside the log is not a large effect except near $y = 0$ and $y = 1$. Since $E_\pi > 10\text{GeV}$, $y > 0.2$. When y becomes close to 1, $\theta_{min} > 1$, the kinematic region is unphysical. Hence we will use the last approximation.

$$\sigma_{\gamma^*P} = \frac{\alpha\sigma_T}{\pi} \ln \frac{Q_{max}}{m_e} \int \frac{dy}{y} [2 - 2y + y^2]$$

$$\sigma_{\gamma^*P} = \frac{\alpha\sigma_T}{\pi} \ln \frac{Q_{max}}{m_e} \left(-2 \ln y_{min} - \frac{3}{2} + 2y_{min} - \frac{1}{2}y_{min}^2\right) \approx 2.2\mu\text{barns}$$

This is much smaller than the photoproduction cross section, so the contribution to the rate is unimportant.

The asymmetry of the virtual photoproduction, however, is larger than for real photons. Using $Q^2 = E^2\theta^2(1 - y)$, we have

$$\int Q^2 d\sigma = \frac{\alpha E^2 \sigma_T}{\pi} \int \int \theta d\theta \frac{dy}{y} [2 - 2y + y^2](1 - y)$$

over all allowed θ and y . The integral over θ is simple and is dominated by θ_{max} :

$$\int Q^2 d\sigma = \frac{\alpha Q_{max}^2 \sigma_T}{\pi} \int \frac{dy}{y} [2 - 2y + y^2]$$

Hence

$$\langle Q^2 \rangle = \frac{Q_{max}^2}{2 \ln(Q_{max}/m_e)} \approx \frac{Q_{max}^2}{15}.$$

This gives $(A\sigma)_{\gamma^*P}/(A\sigma)_{M=7}$, comparable to the case for DIS. This ratio, proportional to $Q_{max}^2 \sim 1 \text{ (GeV/c)}^2$, is very sensitive to the cutoff because of the sensitivity of the asymmetry. We argue below that a cutoff of 0.2 is more realistic.

C.7 Comments

First, we relate the virtual photoproduction to DIS. Starting with

$$\begin{aligned} \frac{d^2\sigma}{dE'd\Omega} &= \frac{\alpha}{2\pi^2 Q^2} \frac{E'}{E} \frac{E^2 + E'^2}{\nu} \sigma_T = \frac{\alpha}{2\pi^2 2M\nu x} \frac{EE'}{\nu} [1 + (1 - y)^2] \sigma_T \\ \frac{d^2\sigma}{dx dy} &= \frac{d^2\sigma}{dE'd\Omega} \frac{2\pi M\nu}{E'} = \frac{\alpha E}{2\pi xy} [1 + (1 - y)^2] \sigma_T \end{aligned}$$

This looks like the DIS case except that the xy in the denominator is not squared. This fact allows for the total cross section to converge; the DIS total cross section if integrated to low Q^2 is high but unphysical. The ratio of the cross sections is

$$\frac{\sigma_{\gamma N}}{\sigma_{DIS}} = \frac{Q^2 \sigma_T}{4\pi F_2}$$

The Q^2 where we switch from DIS to virtual photoproduction should occur when this ratio is unity:

$$Q^2 = \frac{4\pi\alpha F_2}{\sigma_T} \approx 0.2.$$

If the cross sections are reasonable smooth, this cutoff approximation should give an upper bound approximately equal to the correct value.

Each of the processes contributes between 0.2 and 1.0 times our expected uncertainty. Thus, the backgrounds should be manageable. We plan refine our estimates with improved theoretical and experimental input and dedicated background runs.

D Resources

The following list gives a breakdown of the projects needed for this experiment and an assignment of the manpower.

BEAM

Polarized Source	SLAC, Princeton
Laser Systematics Control	Princeton, SLAC
e^- Beam Diagnostic Instrumentation	SLAC
e^- Beam Polarimetry	Temple

TARGET

CalTech

SPECTROMETER

Kent State, SLAC

CALORIMETER

Syracuse

ONLINE

Data Acquisition	Temple, SLAC
ADCs	Princeton
Simultaneous Systematics Calibration	SLAC, Jlab

References

- [1] Y.B. Zel'dovich, JETP **9**, 682 (1959).
- [2] C. Prescott *et al.*, Phys. Lett. B **77**, 347 (1978).
- [3] W. Heil *et al.*, Nucl. Phys. B **327**, 1 (1989).
- [4] P.A. Souder *et al.*, Phys. Rev. Lett. **65**, 694 (1990).
- [5] Musolf, M.J. *et al.* CEBAF preprint TH-93-11, (1993), and references therein.
- [6] E. Derman and W. J. Marciano, Ann. Phys. **121**, 147 (1979).
- [7] A. Czarnecki and W.J. Marciano, Phys. Rev. D **53**, 1066 (1996).
- [8] J. Seeman, Private Communication.
- [9] J.L. Rosner, hep-ph/9704331 (1997), and references therein.
- [10] S. Godfrey, Phys. Rev. D **51**, 1402 (1995),
J.L. Hewett and T.G. Rizzo, Phys. Rep. **183**, 193, (1989).
- [11] E.J. Eichten, K.D. Lane and M.E. Peskin, Phys. Rev. Lett. **50**, 811 (1983).
- [12] B. Schrempp *et al.*, Nucl. Phys. B **296**, 1 (1988).
- [13] J.F. Gunion *et al.*, Phys. Rev. D **40**, 1546, (1989).
- [14] P.D. Acton *et al.*, Phys. Lett. B **295**, 347, (1992).
- [15] M.L. Swartz, Phys. Rev. D **40**, 1521, (1989).
- [16] ALEPH Collaboration, D. Buskulic *et al.*, Z. Phys. C **59**, 215 (1993).
- [17] B.W. Lynn, M.E. Peskin and R.G. Stuart, in *Physics at LEP*, CERN Report No. CERN-86-02 (1986).
- [18] M.E. Peskin and T. Takeuchi, Phys. Rev. D **46**, 381 (1992).
- [19] D.C. Kennedy and B.W. Lynn, Nucl. Phys. **B322**, 1 (1989).
- [20] M.E. Peskin and T. Takeuchi, Phys. Rev. Lett. **65**, 964 (1990).

- [21] I. Maksymyk *et al.* Phys. Rev. **D50**, (1994) 529.
- [22] B. Grinstein and M.B. Wise, Phys. Lett. B **265**, 326, (1991).
- [23] J.L. Hewett *et al.*, SLAC-PUB-7088, (1996).
- [24] B. Mueller et al., Phys. Rev. Lett. 78 (1997) 3824.
- [25] G. G. Petratos *et al.*, SLAC preprint SLAC-PUB-5678 (1991)
- [26] G. G. Petratos, SLAC preprint SLAC-ESA-2-93 (1993)
R. G. Arnold *et al.*, SLAC preprint SLAC-ESA-3-93 (1993).
- [27] Brun, R. *et al.*, GEANT3 Users Guide, CERN/DD/EE/84.1.
- [28] P. Gorodetzky *et al.*, Nucl. Instr. Meth. A **361** (1995) 161,
G. Anzivino *et al.*, Nucl. Instr. Meth. A **357** (1995) 369.
- [29] R.G. Arnold *et al.*, SLAC Proposal E-154, (1993).
- [30] J. Kessler in *Polarized Electrons*, Springer-Verlag, Second Edition, (1985), 137.
- [31] R. Erickson, private communication.
- [32] H.R. Band and R. Prepost, SLCPOL Note 22, 1988.
- [33] M. Peskin, private communication.
- [34] R. Alley et al., Nucl. Instr. Meth. A **365**, 1 (1995).
- [35] See proceedings of the recent *Workshop on Polarized Electron Sources and Low Energy Polarimeters* held in conjunction with SPIN96 at Amsterdam, The Netherlands, September 6–7, 1996.
- [36] M. Woods et al., J. Appl. Phys. **73**, 8531 (1993)
H. Tang et al., SLAC-PUB-6515 (1994).
- [37] R.A. Mair et al., Phys. Lett. A **212**, 231 (1996).
- [38] G.D. Cates et al., Nucl. Inst. Meth. A **278**, 293 (1989).